Non-peer-reviewed EarthArXiv preprint.

Horizontal Strain Rate estimation from InSAR Observations and the Strapdown Method

Alexandru M. Lapadat[1*], Ramon F. Hanssen[1†]

[1]Mathematical Geodesy and Positioning, Delft University of Technology, Stevinweg 1, Delft, Netherlands

Key points

- Strapdown-derived InSAR velocities enable horizontal strain-rate estimation without requiring GNSS velocity constraints
- Method for estimating strain rate and precision while accounting for spatial averaging and nonlinear velocity variation
- Strain rates in Jakarta distinguish bowl-shaped and differential deformation consistent with different subsidence processes

*Mathematical Geodesy and Positioning, Delft University of Technology, Stevinweg 1, Delft, Netherlands; A.M.Lapadat@tudelft.nl

†Mathematical Geodesy and Positioning, Delft University of Technology, Stevinweg 1, Delft, Netherlands; R.F.Hanssen@tudelft.nl

Abstract

Interferometric Synthetic Aperture Radar (InSAR) is able to estimate ground-surface displacements but interpreting deformation mechanisms and infrastructure risk requires analysis of spatial displacement gradients. The recently introduced strapdown method enables three-dimensional displacement velocities to be estimated from InSAR observations alone, including the east and north components required for horizontal strain-rate analysis. Here, we present an approach that inverts these east and north velocity components using a finite-element framework to estimate a continuous horizontal velocity field and subsequently derive the horizontal strain-rate tensor and other deformation metrics with quantified uncertainties. Applied to Jakarta, these results show that horizontal strain-rate analysis can distinguish between two distinctly different mechanisms driving subsidence and identify regions of differential deformation relevant to infrastructure risk. The method enables horizontal deformation to be quantified from InSAR observations alone without requiring external geodetic velocity constraints.

Plain Language Summary

Ground deformation occurs when neighboring parts of Earth's surface move in ways that stretch, compress, or distort the ground. Measuring the rate of this deformation, known as strain rate, helps reveal the processes driving ground motion and identify areas where infrastructure may be affected. Interferometric synthetic aperture radar (InSAR) provides spatially dense measurements of surface motion from space with millimeter-scale sensitivity. However, its satellite viewing geometry reduces the sensitivity to the north component of the motion. The recently developed strapdown method enables north-south motion to be estimated from InSAR observations alone. We present a method that uses strapdown-derived 3D velocities to map horizontal stretching, contraction, and distortion and assess the precision of the estimates. Applied to Jakarta, Indonesia, where land subsidence has been documented for nearly a century, the approach reveals contrasting deformation patterns. Several major subsiding areas show bowl-shaped patterns consistent with deeper sources of subsidence. In Central Jakarta, however, pronounced horizontal distortion occurs despite relatively modest subsidence, which can be an indication of shallower subsidence sources. Our method helps distinguish subsidence-related deformation patterns and identify areas of potential concern for buildings and infrastructure without requiring additional ground-based constraints.

1 Introduction

Geodetic velocity fields describe the motion of the Earth's surface, while their spatial derivatives provide the strain-rate tensor, which quantifies local rates of horizontal extension, shortening, and shear. Early geodetic estimates of strain accumulation and strain rate relied on repeated terrestrial surveys (Savage & Burford, 1970; Welsch, 1986). The development of dense Global Navigation Satellite Systems (GNSS) networks enabled strain-rate fields to be reconstructed from regional to global scales (Shen et al., 1996; Kreemer et al., 2014). Various estimation methods and spatial representations have since been developed, with increasing focus on uncertainty quantification (Shen et al., 2015; Tape et al., 2009; Okazaki et al., 2021; Nozue & Fukahata, 2025). Geodetic strain-rate fields are widely used to study tectonic deformation, seismic hazard, land subsidence, ground fissuring, and differential deformation affecting buildings and infrastructure.

Interferometric Synthetic Aperture Radar (InSAR) provides substantially denser spatial sampling than typical GNSS networks, (Hanssen, 2001), enabling strain-rate estimation at finer spatial scales. However, InSAR measures only the projection of 3D motion onto the radar line of sight (LoS), and near-polar SAR acquisition geometries provide weak sensitivity to north-south motion (Wright et al., 2004). Consequently, LoS velocities are often projected onto the vertical or decomposed into east and up components by assuming

negligible north-oriented motion (Brouwer & Hanssen, 2023). Horizontal strain-rate estimation, however, requires both east and north velocity components. GNSS observations have therefore been used to constrain the poorly observed north–south motion, either by prescribing or interpolating north velocities (Tymofyeyeva & Fialko, 2018; Xu et al., 2021; Weiss et al., 2020; Ou et al., 2022), or by combining GNSS and InSAR observations to reconstruct continuous horizontal velocity fields (Walters et al., 2014; Kim et al., 2026). These approaches have enabled InSAR-based horizontal strain-rate estimation from local to continental scales (Tymofyeyeva & Fialko, 2018; Weiss et al., 2020; Elliott et al., 2026).

A common approach reconstructs the horizontal velocity field using piecewise-linear triangular meshes (Walters et al., 2014; Pagli et al., 2014; Wang et al., 2019). Each velocity observation is treated as a point value used to estimate the velocities at the triangle vertices. Linear interpolation of these estimated vertex velocities produces a constant velocity gradient, and hence a constant strain rate, within each triangle. Representing strain-rate variations over shorter spatial scales therefore requires finer triangulation and correspondingly more unknowns.

Building on the strapdown method of Brouwer and Hanssen (2024), we use its east and north velocity estimates for Regions of Uniform Motion (RUMs). Unlike the velocity observations treated as point values in the approach described above, each RUM velocity represents the average horizontal motion over its area. Applying this point-observation formulation to RUM velocities would require assigning each area average to a representative point, such as the RUM centroid. This assignment is exact at the centroid for a linear velocity field but may introduce errors when the velocity varies nonlinearly. Such errors can distort the reconstructed velocity gradients and derived strain rates. Consistent strain-rate estimation therefore requires an observation model that accounts for the spatial support of each RUM. Moreover, representing nonlinear velocity variation over short spatial scales requires a sufficiently flexible representation of the velocity field.

Here, we develop an InSAR-only method for estimating horizontal strain-rate fields from strapdown-derived east and north RUM velocities without requiring additional GNSS velocity constraints. The domain is discretized using eight-node quadratic quadrilateral (Q8) finite elements, constructed such that each observed RUM coincides with one element. Quadratic interpolation of the unknown nodal velocities allows nonlinear velocity variation over short spatial scales, while an observation model formulated for RUM velocities accounts for their spatial support through area averaging. Weighted Tikhonov regularization is then used to estimate these nodal velocities, from which element-averaged horizontal strain-rate tensors and derived strain-rate quantities are computed, with uncertainties propagated from the input RUM velocity covariance information. We demonstrate the method using an InSAR-derived 3D RUM velocity field spanning 2014–2025 over Jakarta, with 450 × 450 m RUMs.

The remainder of the paper is organized as follows. Sec. 2 introduces the mathematical background on horizontal deformation and strain rate. Sec. 3 presents the estimation method. Sec. 4 applies the method to Jakarta and assesses the resulting strain-rate fields, their precision, and consistency. Sec. 5 discusses the deformation patterns, the performance and limitations of the method, followed by the conclusions in Sec 6.

2 Background: Horizontal deformation and strain-rate quantities

Displacements and velocities describe how points move through space. A horizontal velocity field can be described by $\big(v_x(x,y), v_y(x,y)\big)$, where v_x and v_y are the velocity components along two arbitrary orthogonal horizontal coordinate directions at location (x, y). Together, these components define the horizontal velocity field

$$\mathbf{v}(x,y) = \begin{bmatrix} v_x(x,y) \\ v_y(x,y) \end{bmatrix}, \tag{1}$$

where the bold-faced notation $\mathbf{v}$ denotes the vector field. Whereas displacement and velocity describe motion, *deformation* describes spatial differences in that motion that change the shape or size of a finite ground-surface area. Such deformation occurs when points within an area undergo different displacements, changing their relative distances and/or orientations. Changes in relative distances produce *normal strain*, i.e., extension or shortening, whereas changes in relative orientation produce *shear strain*, i.e., angular distortion. Because geodetic displacement observations do not provide the pre-existing strain state, deformation is typically described through its temporal rate of change, i.e., the *strain rate*, which is derived from the velocity field.

The spatial variation of the horizontal velocity field in Eq. (1) is described by the velocity-gradient tensor

$$\nabla \mathbf{v} = \begin{bmatrix} \dfrac{\partial v_x}{\partial x} & \dfrac{\partial v_x}{\partial y} \\ \dfrac{\partial v_y}{\partial x} & \dfrac{\partial v_y}{\partial y} \end{bmatrix}, \tag{2}$$

which contains deformation rates and rigid-body rotation rates; translation is eliminated by spatial differentiation. These contributions are separated into the symmetric and antisymmetric parts of the velocity-gradient tensor,

$$\nabla \mathbf{v} = \frac{1}{2}\left(\nabla \mathbf{v} + (\nabla \mathbf{v})^T\right) + \frac{1}{2}\left(\nabla \mathbf{v} - (\nabla \mathbf{v})^T\right) = \dot{\boldsymbol{\varepsilon}} + \boldsymbol{W}, \tag{3}$$

where the symmetric component $\dot{\boldsymbol{\varepsilon}}$ represents the deformation rate, and the antisymmetric component $\boldsymbol{W}$ the rigid-body rotation rate.

For the small deformations typically encountered in geodetic applications, the infinitesimal-strain approximation is adopted, under which higher-order deformation terms are neglected. The horizontal strain-rate tensor is therefore given by the symmetric part of the velocity-gradient tensor,

$$\begin{aligned} \dot{\boldsymbol{\varepsilon}} &= \frac{1}{2}\left(\nabla \mathbf{v} + (\nabla \mathbf{v})^T\right) \\ &= \begin{bmatrix} \dfrac{\partial v_x}{\partial x} & \dfrac{1}{2}\left(\dfrac{\partial v_x}{\partial y} + \dfrac{\partial v_y}{\partial x}\right) \\ \dfrac{1}{2}\left(\dfrac{\partial v_x}{\partial y} + \dfrac{\partial v_y}{\partial x}\right) & \dfrac{\partial v_y}{\partial y} \end{bmatrix} = \begin{bmatrix} \dot{\varepsilon}_{xx} & \dot{\varepsilon}_{xy} \\ \dot{\varepsilon}_{xy} & \dot{\varepsilon}_{yy} \end{bmatrix}. \end{aligned} \tag{4}$$

The diagonal components, $\dot{\varepsilon}_{xx}$ and $\dot{\varepsilon}_{yy}$, are the normal strain rates along the x- and y-directions, respectively. Positive values indicate extension and negative values shortening along the corresponding direction. The off-diagonal component, $\dot{\varepsilon}_{xy}$, is the tensorial shear strain rate and equals one half of the engineering shear strain rate,

$$\dot{\gamma}_{xy} = \left(\frac{\partial v_x}{\partial y} + \frac{\partial v_y}{\partial x}\right), \tag{5}$$

which describes the rate of angular distortion between material lines initially aligned with the x- and y-directions. All strain-rate components have units of inverse time.

Because the normal and shear components are defined relative to the x-y axes, their numerical values depend on the selected horizontal coordinate system. Rotating the coordinate axes changes the tensor components, but not the underlying physical deformation. Since geodetic horizontal velocities are conventionally expressed in an east-north (E-N) coordinate system, we take $x = \mathrm{E}$ and $y = \mathrm{N}$, such that $v_x = v_\mathrm{E}$ and $v_y = v_\mathrm{N}$. The corresponding strain-rate components are denoted by $\dot{\varepsilon}_{\mathrm{EE}}$, $\dot{\varepsilon}_{\mathrm{NN}}$, and $\dot{\varepsilon}_{\mathrm{EN}}$.

At each location, the horizontal strain-rate tensor defines two orthogonal principal directions along which the normal strain rate attains its maximum and minimum values. Aligning the coordinate axes with these directions eliminates the shear component and defines the *principal strain-rate coordinate system*. As illustrated in Fig. 1 (top), when the

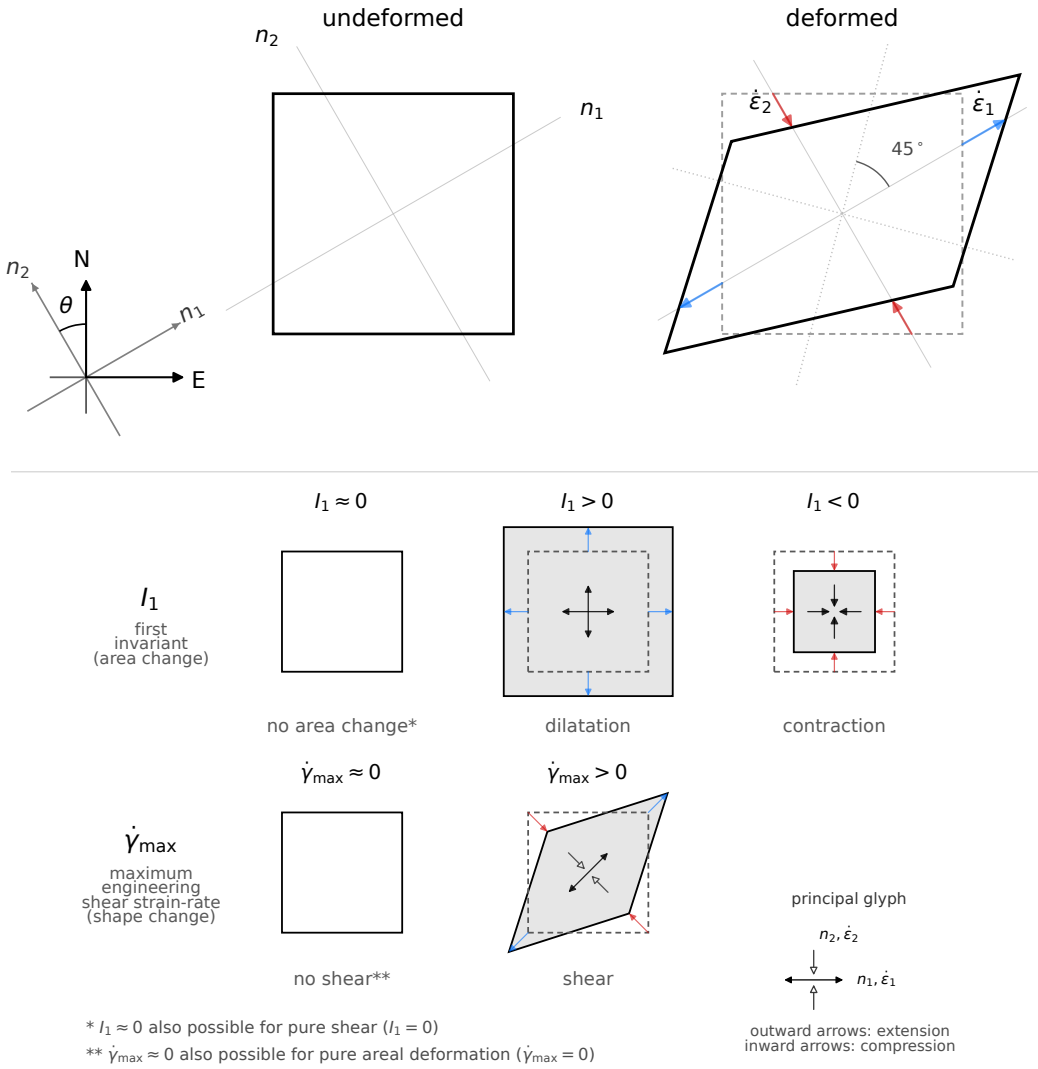


Figure 1. Schematic illustration of horizontal strain-rate quantities. **Top:** The same deformation expressed in the east-north (E-N) and principal strain-rate (n_1-n_2) coordinate systems. In the latter, the shear component vanishes, leaving only the principal strain rates ($\dot{\varepsilon}_1$) and ($\dot{\varepsilon}_2$). **Bottom:** Idealized deformation states for the first invariant I_1, representing horizontal areal dilatation or contraction, and the maximum engineering shear strain rate $\dot{\gamma}_{\max}$ representing angular distortion.

principal directions are not aligned with E–N, an initially square area with sides aligned with the E–N axes generally deforms into a parallelogram. In the E–N coordinate system, this deformation is represented by both normal and shear strain-rate components. In the principal coordinate system, the same deformation is represented solely by the principal strain rates $\dot{\varepsilon}_1$ and $\dot{\varepsilon}_2$ along the orthogonal directions n_1 and n_2, respectively.

These directions are the eigenvectors of $\dot{\boldsymbol{\varepsilon}}$, and the corresponding eigenvalues are

$$\dot{\varepsilon}_{1,2} = \frac{1}{2}\left[\dot{\varepsilon}_{\mathrm{EE}} + \dot{\varepsilon}_{\mathrm{NN}} \pm \sqrt{\left(\dot{\varepsilon}_{\mathrm{EE}} - \dot{\varepsilon}_{\mathrm{NN}}\right)^2 + 4\dot{\varepsilon}_{\mathrm{EN}}^2}\right], \qquad \dot{\varepsilon}_1 \geq \dot{\varepsilon}_2, \tag{6}$$

where $\dot{\varepsilon}_1$ and $\dot{\varepsilon}_2$ are the maximum and minimum normal strain rates along n_1 and n_2, respectively. Together, the principal strain rates and directions characterize the normal deformation and the orientations along which the strongest extension or shortening occurs, providing a direct measure of the directional character of the deformation.

To facilitate mapping, comparison, and spatial interpretation, the principal strain rates and their directions can be complemented with scalar measures that are independent of the selected coordinate system. The first invariant I_1 quantifies areal deformation, whereas the maximum engineering shear strain rate $\dot{\gamma}_{\max}$ quantifies distortional deformation, see Fig. 1 (bottom).

The first invariant is the trace of the strain-rate tensor,

$$I_1 = \mathrm{tr}\left(\dot{\boldsymbol{\varepsilon}}\right) = \dot{\varepsilon}_{\mathrm{EE}} + \dot{\varepsilon}_{\mathrm{NN}} = \dot{\varepsilon}_1 + \dot{\varepsilon}_2, \tag{7}$$

and represents the fractional rate of change of horizontal area, or dilatation rate (Savage et al., 2001). Positive values ($I_1 > 0$) indicate expansion (dilatation), whereas negative values ($I_1 < 0$) indicate contraction. Spatial patterns in I_1 therefore identify where the ground surface expands or contracts and can help interpret the geometry and possible mechanism of the deformation.

Distortional deformation is quantified by the maximum engineering shear strain rate,

$$\dot{\gamma}_{\max} = \sqrt{\left(\dot{\varepsilon}_{\mathrm{EE}} - \dot{\varepsilon}_{\mathrm{NN}}\right)^2 + 4\dot{\varepsilon}_{\mathrm{EN}}^2} = \dot{\varepsilon}_1 - \dot{\varepsilon}_2, \tag{8}$$

which represents the maximum rate of angular distortion, i.e., the greatest rate at which an initially right angle changes. This maximum occurs along directions rotated by 45° with respect to the principal directions, see Fig. 1 (bottom). Large values of $\dot{\gamma}_{\max}$ identify areas of strong differential deformation and are therefore particularly relevant for assessing potential deformation-induced effects on buildings and linear infrastructure.

All strain-rate quantities introduced above are derived from spatial derivatives of the horizontal velocity field. The practical challenge is therefore to obtain stable spatial derivatives from the strapdown velocities, which represent spatial averages over discrete RUMs, rather than point samples of a continuous velocity field. Direct differentiation of neighboring RUM velocities would make the resulting strain-rate estimates sensitive to observational noise and abrupt RUM-to-RUM velocity differences. This motivates the finite-element Tikhonov estimation presented in the following section, which reconstructs a continuous horizontal velocity field from the RUM velocities and spatially differentiates this field to obtain the strain-rate tensor and derived deformation quantities.

3 Methodology

The objective is to derive a continuous horizontal strain-rate field from the east and north RUM velocities obtained by the strapdown decomposition, while propagating their uncertainties and correlations. Two characteristics of the RUM velocity observations must be accounted for. One is that the velocities are available only for discrete RUMs, whereas strain-rate estimation requires spatial derivatives of a continuous horizontal velocity field. The other is that each RUM velocity represents the area-averaged motion over its area

rather than the velocity at a single point. The estimation framework therefore reconstructs a continuous horizontal velocity field while explicitly accounting for the spatial support of the RUM observations.

The methodology consists of four steps. First, the domain is discretized using a finite-element mesh, with the east and north nodal velocities as unknowns. Second, an observation model relates these nodal velocities to the observed RUM velocities by averaging the interpolated velocity field over each RUM. Third, the nodal velocities are estimated using weighted Tikhonov regularization, incorporating the RUM velocity variance–covariance information. Finally, the estimated velocity field is spatially differentiated and area-averaged to obtain the horizontal strain-rate tensor for each finite element, from which the derived strain-rate quantities and their uncertainties are computed.

3.1 Finite-element representation of the horizontal velocity field

The first step uses a finite-element mesh to construct a continuous finite-element representation of the horizontal velocity field. A continuous representation is needed because horizontal strain rates require spatial derivatives of the horizontal velocity field, whereas the strapdown decomposition provides discrete estimates of east and north RUM velocities (Brouwer & Hanssen, 2023, 2024).

Computing velocity derivatives by directly differencing neighboring RUM velocities can amplify their uncertainties and produce large local gradients where abrupt velocity differences occur, resulting in noisy strain-rate estimates.

Fig. 2 shows the finite-element mesh, which is constructed such that each observed RUM

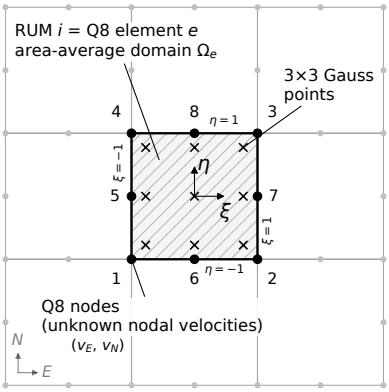


Figure 2. Finite-element representation of the horizontal velocity field. The hatched square represents a RUM, coinciding with one finite element of domain Ω_e. Each element uses eight-node quadratic quadrilateral (Q8) interpolation, with unknown east and north velocities at the four corner and four midside nodes (black dots). Adjacent elements share boundary nodes, ensuring continuity of the interpolated velocity field. Black crosses indicate the (3×3) Gauss points used for numerical integration.

(hatched square) corresponds to a finite element of the same spatial extent. Because RUM velocity estimates are available only at selected locations, the mesh also contains elements without RUM observations to maintain spatial connectivity across the domain. The velocity field is represented using eight-node quadratic quadrilateral (Q8) elements, with four corner and four midside nodes. The east and north velocity components at the mesh nodes are the

estimation unknowns. Adjacent elements share their boundary nodes and therefore share the corresponding nodal velocity unknowns.

Each finite element e has eight nodes, indexed by $a = 1, \ldots, 8$. The horizontal velocity field within the element is represented by quadratic interpolation of the unknown nodal velocities,

$$\mathbf{v}_e(\xi, \eta) = \sum_{a=1}^{8} N_a(\xi, \eta)\mathbf{v}_a, \tag{9}$$

where $(\xi, \eta) \in [-1, 1] \times [-1, 1]$ are the local element coordinates, $N_a(\xi, \eta)$ is the quadratic shape function associated with node a (see App. S1.1), and $\mathbf{v}_a = [v_{\mathrm{E},a}, v_{\mathrm{N},a}]^T$ contains the unknown east and north velocity components at that node.

Adjacent elements share their boundary nodes and corresponding nodal velocity unknowns, ensuring continuity of the interpolated horizontal velocity field across the entire mesh. The next step relates the nodal velocity unknowns to the observed area-averaged RUM velocities.

3.2 Observation model relating nodal velocities to RUM velocities

The second step formulates the observation model relating the unknown nodal velocities to the observed RUM velocities. Whereas Eq. (9) provides the horizontal velocity at any location within a finite element, each RUM observation represents the average horizontal velocity over the corresponding RUM area. The observation model therefore averages the interpolated velocity field over the same region, ensuring that the modeled and observed velocities have the same spatial support.

For each observed RUM i, element e denotes the corresponding finite element. Averaging the interpolated velocity field over this element gives

$$\hat{\mathbf{y}}_i = \frac{1}{|\Omega_e|} \int_{\Omega_e} \mathbf{v}_e(\xi, \eta)\, \mathrm{d}\Omega = \sum_{a=1}^{8} \bar{N}_{a,e}\, \mathbf{v}_a, \tag{10}$$

where Ω_e denotes the domain of element e, $|\Omega_e|$ its area, and $\bar{N}_{a,e}$ the area average of shape function N_a over the element. The integral is evaluated numerically using 3×3 Gauss quadrature (Bathe, 1996). The velocity field is evaluated at the nine Gauss points (black crosses in Fig. 2). The explicit quadrature formulation is given in App. S1.2.

Stacking the observed RUM velocities and nodal velocity unknowns with all east components followed by all north components gives the observation model

$$\begin{bmatrix} \underline{\mathbf{y}}_{\mathrm{E}} \\ \underline{\mathbf{y}}_{\mathrm{N}} \end{bmatrix} = \begin{bmatrix} \mathbf{A}_{\mathrm{E}} & \mathbf{0} \\ \mathbf{0} & \mathbf{A}_{\mathrm{N}} \end{bmatrix} \begin{bmatrix} \mathbf{x}_{\mathrm{E}} \\ \mathbf{x}_{\mathrm{N}} \end{bmatrix} + \begin{bmatrix} \underline{\eta}_{\mathrm{E}} \\ \underline{\eta}_{\mathrm{N}} \end{bmatrix} \tag{11}$$

where $\mathbf{A} = \mathrm{diag}(\mathbf{A}_{\mathrm{E}}, \mathbf{A}_{\mathrm{N}})$ maps the nodal velocity unknowns to the area-averaged RUM velocities, and $\underline{\boldsymbol{\eta}}$ contains the observation errors. The blocks $\mathbf{A}_{\mathrm{E}}$ and $\mathbf{A}_{\mathrm{N}}$ are assembled from the area-averaged shape functions $\bar{N}_{a,e}$ of the elements associated with RUM observations; their explicit construction is given in App. S1.2.

The observation errors are assumed to have zero mean and variance-covariance matrix $\mathbf{Q}_{yy}$, which retains the east-north covariance within each RUM and assumes zero covariance between different RUMs (Brouwer & Hanssen, 2023, 2024). The corresponding weight matrix is $\mathbf{W} = \mathbf{Q}_{yy}^{-1}$. The observation model and weight matrix are used in the next step to estimate the nodal velocities by weighted Tikhonov regularization.

3.3 Regularized estimation of the nodal velocities

The third step estimates the unknown nodal velocities from the RUM observations using weighted Tikhonov regularization. Regularization is needed because the finite-element

representation contains more nodal velocity unknowns than observed RUM velocity components, so the nodal velocities cannot be uniquely determined from the observations alone. This non-uniqueness permits solutions with large local velocity gradients that are weakly constrained by the observations, and would consequently produce an unrealistically rough strain-rate field.

To stabilize the estimation and suppress poorly constrained spatial variability, the weighted Tikhonov formulation uses a regularization operator $\mathbf{L}$ comprising two complementary terms,

$$\mathbf{L} = \begin{bmatrix} \mathbf{L}_v \\ \mathbf{L}_{\dot{\varepsilon}\to x} \end{bmatrix}, \tag{12}$$

where $\mathbf{L}_v$ penalizes spatial variations in velocity gradients, while $\mathbf{L}_{\dot{\varepsilon}\to x}$ penalizes differences in the element-averaged horizontal strain-rate tensors between neighboring elements.

The velocity regularization $\mathbf{L}_v$ is constructed from the spatial derivatives of the quadratic shape functions, $\partial N_a/\partial \mathrm{E}$ and $\partial N_a/\partial \mathrm{N}$, and thereby penalizes rapid spatial variations in velocity gradients in the interpolated field.

The second regularization term promotes similarity between the strain-rate tensors of nearby elements with similar deformation characteristics through coupling that weakens as their spatial separation or deformation dissimilarity increases. The neighborhood $\mathcal{N}_e$ of element e comprises all elements k whose centroid-to-centroid distance d_{ek} does not exceed a prescribed threshold d_{thresh}. For each pair e and $k \in \mathcal{N}_e$, a coupling weight w_{ek} is assigned as the product of a distance factor w_{dist} and a deformation-similarity factor $w_{\dot{\varepsilon}}$.

The distance factor w_{dist} depends on d_{ek} relative to d_{thresh}, whereas the deformation-similarity factor $w_{\dot{\varepsilon}}$ depends on differences in principal strain rates. Because the strain-rate field is not yet available, a proxy strain-rate tensor is obtained for each element by fitting a planar velocity field to nearby RUM velocities within d_{thresh} of its centroid. The resulting proxy principal strain rates are used solely to determine the deformation-similarity factor $w_{\dot{\varepsilon}}$, and are not estimation unknowns. The coupling weight and its distance and deformation-similarity factors are defined as

$$w_{ek} = w_{\mathrm{dist}}\, w_{\dot{\varepsilon}}, \qquad w_{\mathrm{dist}} = \frac{1}{1 + (d_{ek}/d_{\mathrm{thresh}})^2}, \qquad w_{\dot{\varepsilon}} = \exp\!\left(-\frac{\Delta\lambda_{ek}^2}{\sigma_{\dot{\varepsilon}}^2}\right). \tag{13}$$

Here, $\Delta\lambda_{ek}$ is the Euclidean distance between the proxy principal strain-rate vectors of elements e and k, and $\sigma_{\dot{\varepsilon}}$ is estimated from the median absolute deviation of $\Delta\lambda_{ek}$ over all considered element pairs. Hence, w_{ek} is largest for spatially close elements with similar proxy principal strain rates and decreases with increasing spatial separation or increasing differences in the proxy principal strain rates.

These coupling weights define the strain-rate regularization matrix $\mathbf{L}_{\dot{\varepsilon}}$, which acts on the components of the element-averaged strain-rate tensors. Because the estimation unknowns are the nodal velocities rather than these strain-rate components, the regularization is mapped to nodal-velocity space as

$$\mathbf{L}_{\dot{\varepsilon}\to x} = \mathbf{L}_{\dot{\varepsilon}}\mathbf{B}, \tag{14}$$

where $\mathbf{B}$ maps the nodal velocities to the element-averaged strain-rate components, as detailed in Sec. 3.4.

Before combining the two regularization terms $\mathbf{L}_v$ and $\mathbf{L}_{\dot{\varepsilon}\to x}$ in $\mathbf{L}$, the two terms are normalized to comparable scales to prevent either from dominating the regularization solely because of differences in magnitude. Their explicit construction and normalization, including the planar fits used to derive the proxy strain rates, are given in App. S1.3.

With the observation model $\mathbf{A}$, weight matrix $\mathbf{W}$, and regularization operator $\mathbf{L}$ defined, the nodal velocities are estimated using weighted Tikhonov regularization (Aster et

al., 2018; Tarantola, 2005),

$$\hat{\underline{\mathbf{x}}} = \arg\min_{\mathbf{x}} \left\| \mathbf{W}^{1/2} \left(\mathbf{A}\mathbf{x} - \underline{\mathbf{y}} \right) \right\|_2^2 + \alpha^2 \left\| \mathbf{L}\mathbf{x} \right\|_2^2, \tag{15}$$

where the first term measures the weighted observation residual and the second term imposes the regularization defined by $\mathbf{L}$. The regularization parameter $\alpha > 0$ controls the balance between the observation fit and the imposed regularization. For a fixed α, the estimated nodal velocities satisfy the normal equation

$$\left(\mathbf{A}^T\mathbf{W}\mathbf{A} + \alpha^2 \mathbf{L}^T\mathbf{L} \right) \hat{\underline{\mathbf{x}}} = \mathbf{A}^T\mathbf{W}\underline{\mathbf{y}}. \tag{16}$$

The regularization parameter α is selected using the Morozov discrepancy principle (Nair et al., 2003; Anzengruber & Ramlau, 2010; Ding et al., 2026), which chooses α such that the squared weighted residual norm is consistent with the assumed observation-error model. With $\mathbf{W} = \mathbf{Q}_{yy}^{-1}$ and $2n_r$ observed horizontal velocity components, the target squared weighted residual norm is $2n_r$. Hence, the selected α satisfies

$$\left\| \mathbf{W}^{1/2} \left(\mathbf{A}\hat{\underline{\mathbf{x}}} - \underline{\mathbf{y}} \right) \right\|_2^2 = 2n_r. \tag{17}$$

The variance–covariance matrix of the estimated nodal velocities, obtained by propagating the covariance of the observed RUM velocities through the regularized estimator, is

$$\mathbf{Q}_{\hat{x}} = \left(\mathbf{A}^T\mathbf{W}\mathbf{A} + \alpha^2 \mathbf{L}^T\mathbf{L} \right)^{-1} \mathbf{A}^T\mathbf{W}\mathbf{A} \left(\mathbf{A}^T\mathbf{W}\mathbf{A} + \alpha^2 \mathbf{L}^T\mathbf{L} \right)^{-1}. \tag{18}$$

This covariance quantifies the uncertainty propagated from the RUM velocity covariance $\mathbf{Q}_{yy}$, conditional on the selected α and $\mathbf{L}$.

Substituting the estimated nodal velocities $\hat{\underline{\mathbf{x}}}$ into the observation model in Eq. (11) gives the fitted RUM velocities, $\hat{\underline{\mathbf{y}}} = \mathbf{A}\hat{\underline{\mathbf{x}}}$. Interpolation of $\hat{\underline{\mathbf{x}}}$ using Eq. (9) yields the estimated continuous horizontal velocity field.

3.4 Strain-rate field derivation and uncertainty propagation

The final step derives element-averaged horizontal strain-rate tensors from the estimated continuous horizontal velocity field and computes the strain-rate quantities $(\hat{I}_1, \widehat{\dot{\gamma}}_{\max}, \hat{\dot{\varepsilon}}_{1,2})$ with their associated uncertainties. For each finite element, the strain-rate tensor is derived from the spatial derivatives of the horizontal velocity field, after which the resulting strain-rate components are averaged over the element.

The velocity derivatives are obtained by differentiating the quadratic shape functions N_a in Eq. (9) with respect to the physical east and north coordinates. These derivatives are evaluated at the nine Gauss points shown in Fig. 2 and combined according to Eq. (4) to obtain the normal strain-rate components $\dot{\varepsilon}_{\mathrm{EE}}$ and $\dot{\varepsilon}_{\mathrm{NN}}$ and the shear strain-rate component $\dot{\varepsilon}_{\mathrm{EN}}$.

These three components are then averaged over the element using 3×3 Gauss quadrature to form the element-averaged horizontal strain-rate tensor. For element e, this tensor is

$$\widehat{\dot{\boldsymbol{\varepsilon}}}_e = \frac{1}{|\Omega_e|} \int_{\Omega_e} \begin{bmatrix} \dfrac{\partial \hat{v}_{\mathrm{E}}}{\partial \mathrm{E}} & \dfrac{1}{2}\left(\dfrac{\partial \hat{v}_{\mathrm{E}}}{\partial \mathrm{N}} + \dfrac{\partial \hat{v}_{\mathrm{N}}}{\partial \mathrm{E}} \right) \\ \dfrac{1}{2}\left(\dfrac{\partial \hat{v}_{\mathrm{E}}}{\partial \mathrm{N}} + \dfrac{\partial \hat{v}_{\mathrm{N}}}{\partial \mathrm{E}} \right) & \dfrac{\partial \hat{v}_{\mathrm{N}}}{\partial \mathrm{N}} \end{bmatrix} \mathrm{d}\Omega = \begin{bmatrix} \hat{\dot{\varepsilon}}_{\mathrm{EE}} & \hat{\dot{\varepsilon}}_{\mathrm{EN}} \\ \hat{\dot{\varepsilon}}_{\mathrm{EN}} & \hat{\dot{\varepsilon}}_{\mathrm{NN}} \end{bmatrix}. \tag{19}$$

Because the tensor in Eq. (19) is symmetric, it is fully described by the three independent components: $(\hat{\dot{\varepsilon}}_{\mathrm{EE}}, \hat{\dot{\varepsilon}}_{\mathrm{NN}}, \hat{\dot{\varepsilon}}_{\mathrm{EN}})$. Interpolation, spatial differentiation, and Gauss averaging are all linear operations and can therefore be combined into a single linear mapping from the nodal velocities to these element-averaged strain-rate components. For element e,

$$\left[\hat{\dot{\varepsilon}}_{\mathrm{EE}} \; \hat{\dot{\varepsilon}}_{\mathrm{NN}} \; \hat{\dot{\varepsilon}}_{\mathrm{EN}} \right]^T = \mathbf{B}_e \hat{\mathbf{x}}_e, \tag{20}$$

where $\hat{\mathbf{x}}_e$ contains the estimated east and north nodal velocities of element e, and $\mathbf{B}_e$ is the corresponding strain-rate mapping matrix. Assembling $\mathbf{B}_e$ over all elements gives the global matrix $\mathbf{B}$, which maps the complete vector of estimated nodal velocities to the element-averaged strain-rate components over the finite-element mesh. The construction and assembly of $\mathbf{B}_e$ and $\mathbf{B}$ are elaborated in App. S1.3.

From each element-averaged horizontal strain-rate tensor, the principal strain rates $\hat{\dot{\varepsilon}}_{1,2}$, the first invariant $\hat{I}_1$, and the maximum engineering shear strain rate $\widehat{\dot{\gamma}}_{\max}$ are computed using Eqs. (6)–(8). Their uncertainties are propagated in two stages. First, the covariance matrix of the estimated nodal velocities, $\mathbf{Q}_{\hat{x}}$ in Eq. (18), is propagated through the linear mapping $\mathbf{B}$ to obtain the covariance matrix of the element-averaged strain-rate components,

$$\mathbf{Q}_{\hat{\dot{\varepsilon}}} = \mathbf{B}\mathbf{Q}_{\hat{x}}\mathbf{B}^T. \tag{21}$$

For each finite element, the corresponding 3×3 block on the diagonal of $\mathbf{Q}_{\hat{\dot{\varepsilon}}}$ contains the variances and covariances of its three strain-rate components. In the second stage, the uncertainties of $\hat{\dot{\varepsilon}}_{1,2}$, $\hat{I}_1$, and $\widehat{\dot{\gamma}}_{\max}$ are obtained from these element-specific covariance matrices by first-order Taylor linearization. The Jacobian of each derived quantity with respect to the three element-averaged strain-rate components is used for covariance propagation; the explicit Jacobians are given in App. S1.4.

The spatial patterns of the resulting strain-rate quantities ($\hat{I}_1, \widehat{\dot{\gamma}}_{\max}, \hat{\dot{\varepsilon}}_{1,2}$) and their propagated uncertainties are analyzed in the following section for Jakarta, Indonesia.

4 Application and results for Jakarta

We apply the proposed methodology to the Jakarta metropolitan area to derive horizontal strain-rate quantities from the InSAR-derived RUM velocity field and assess their precision and internal consistency.

4.1 Data and analysis setup

Jakarta, the world's largest megacity (UN, 2025), is a major land-subsidence hotspot, where subsidence has been documented for almost a century (Schepers, 1926). InSAR studies have revealed strong spatial variability, with localized subsidence bowls superimposed on broader regional subsidence (Abidin et al., 2005; Ng et al., 2012; Koudogbo et al., 2012; Chaussard et al., 2013; Widodo et al., 2019; Harintaka et al., 2024; Sidiq et al., 2025; Lapadat et al., 2026). This makes Jakarta well suited for examining horizontal velocity gradients and associated strain-rate patterns, particularly in densely built-up areas where differential ground deformation may affect buildings and infrastructure.

We apply the proposed method to the InSAR-derived 3D RUM velocity field of Lapadat et al. (2026), covering October 2014–June 2025 (10.7 years) with a spatial discretization of 450×450 m. The field contains 4779 observed RUMs with east and north velocity observations, which are used in the Tikhonov estimation together with their variance–covariance information. The complete 3D RUM velocity dataset is available from (Lapadat & Hanssen, 2025). The input RUM velocity field is shown in Fig. 3. Each RUM is represented by one finite element with identical boundaries, forming a finite-element mesh of 6650 elements. Additional elements without associated RUM observations are included across gaps in RUM coverage to keep the finite-element mesh connected and maintain a continuous velocity-field representation.

To select the spatial extent for the strain-rate regularization, a spherical variogram is fitted to the first invariant (I_1) of the proxy strain-rate tensors, yielding a variogram range of $\sim$1770 m. Because deformation patterns may change over relatively short distances within subsidence regions, we selected a shorter centroid-to-centroid distance threshold of three RUM widths, i.e., $d_{\text{thresh}} = 1350$ m. This limits regularization across deformation transitions and reduces attenuation of localized strain-rate amplitudes.

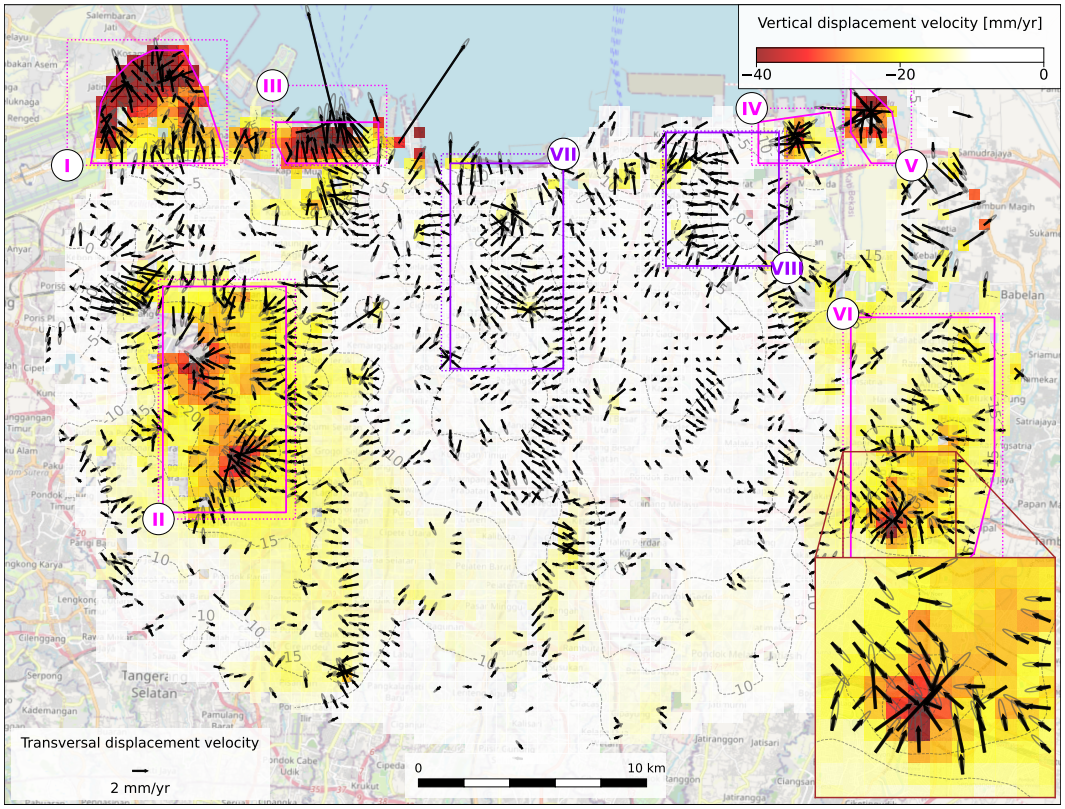


Figure 3. InSAR-derived 3D RUM velocity field of the Jakarta metropolitan area (2014–2025), adapted from Lapadat et al. (2026), and used as input to the strain-rate estimation. Vertical velocities are shown by color. For clarity, only a subset of the horizontal velocity vectors whose magnitudes exceed their 2σ uncertainties is displayed, together with their 2σ confidence ellipses (see the enlarged inset in the lower-right corner). Dashed contours show the iso-displacement lines to which the transversal horizontal velocity vectors are perpendicular. Dashed contours in subsequent figures represent the same iso-displacement lines. Magenta outlines mark the six major subsidence regions (I–VI) identified in Lapadat et al. (2026), while purple outlines mark regions VII–VIII in Central Jakarta, which exhibit pronounced spatial variation in the horizontal velocity field.

Table 1. Strain-rate quantities for the outlined areas in Fig. 4. $\hat{I}_1$: first invariant (areal strain rate); $\widehat{\gamma}_{\max}$: maximum engineering shear strain rate (maximum angular distortion rate); $\hat{\varepsilon}_{1,2}$: principal strain rates (maximum and minimum normal strain rates). Extrema are computed independently within each region and do not necessarily occur at the same RUM location.

Strain-rate quantities								
Region	**# RUMs**	$\hat{I}_1$ [$\mu\varepsilon$/yr]		$\widehat{\gamma}_{\max}$ [$\mu\varepsilon$/yr]	$\hat{\varepsilon}_1$ [$\mu\varepsilon$/yr]		$\hat{\varepsilon}_2$ [$\mu\varepsilon$/yr]	
		min	**max**	**max**	**min**	**max**	**min**	**max**
I	121	−1.2	0.4	0.7	−0.5	0.4	−0.7	0.1
II	299	−0.7	0.2	0.7	−0.3	0.3	−0.6	0.0
III	46	−0.3	1.0	1.0	0.1	0.7	−0.7	0.4
IV	41	−0.5	0.5	0.9	−0.1	0.7	−0.4	−0.0
V	38	−0.4	1.4	0.9	−0.2	1.2	−0.3	0.2
VI	360	−0.5	0.3	0.4	−0.2	0.2	−0.3	0.1
VII	263	−1.4	1.5	1.8	−0.4	1.5	−1.3	0.6
VIII	152	−1.0	1.8	1.4	−0.3	1.4	−1.1	0.6

Since Jakarta had only one long-term GNSS station operating during the 2014–2025 study period (Lapadat et al., 2026), there is no independent validation for the derived spatial variability of the strain-rate field. We therefore assess the precision and internal consistency of the results using two diagnostics: (i) the propagated strain-rate uncertainties, (ii) residuals between the observed and fitted RUM velocities.

4.2 Horizontal strain-rate field

Fig. 4 shows the spatial distributions of the first invariant $\hat{I}_1$ and the maximum engineering shear strain rate $\widehat{\gamma}_{\max}$ across Jakarta. Principal strain-rate glyphs are superimposed in Fig. 4a, to show the orientations and relative magnitudes of the maximum and minimum principal strain rates. Only scalar estimates whose magnitudes exceed twice their propagated standard deviation are shown.

In several of the major subsidence regions (I–VI) previously identified from the InSAR-derived 3D RUM velocity field of Jakarta (Lapadat et al., 2026), negative $\hat{I}_1$ (indicating areal contraction) occurs near the region centers, accompanied by inward-oriented principal shortening glyphs. Positive $\hat{I}_1$ occurs along parts of the outer flanks and surrounding areas, see Fig. 4a. Several of these flanks also show large maximum engineering shear strain rates $\widehat{\gamma}_{\max}$, particularly near transitions between contraction and dilatation, see Fig. 4b. This pattern is particularly apparent in the southern part of region II. In contrast, two areas in Central Jakarta, labeled VII and VIII, show elongated patterns of alternating contraction and dilatation, accompanied by locally large maximum engineering shear strain rates.

Tab. 1 quantifies the spatial variability evident in Fig. 4. Most regions contain both contraction ($\hat{I}_1 < 0$) and dilatation ($\hat{I}_1 > 0$), demonstrating that the horizontal deformation varies spatially within the subsidence regions. Yet, it is striking that the range of the areal deformation $\hat{I}_1$ within regions VII and VIII is 2.9 and 2.8 $\mu\varepsilon$/yr, respectively, which is more than twice the average range of 1.23 $\mu\varepsilon$/yr across the six other subsidence regions (I–VI). Moreover, the maximum engineering shear strain rate $\hat{\gamma}_{\max}$ in regions VII and VIII is 1.8 and 1.4 $\mu\varepsilon$/yr, respectively, approximately twice the average regional maximum of 0.77 $\mu\varepsilon$/yr across the six other subsidence regions (I–VI). The distinctly larger spatial variation in areal strain rate and angular distortion in regions VII and VIII indicates a different deformation pattern, potentially reflecting differences in the underlying deformation mechanism. Cumulative strain values for the 10.7-year observation period can be easily derived by multiplication with the time interval.

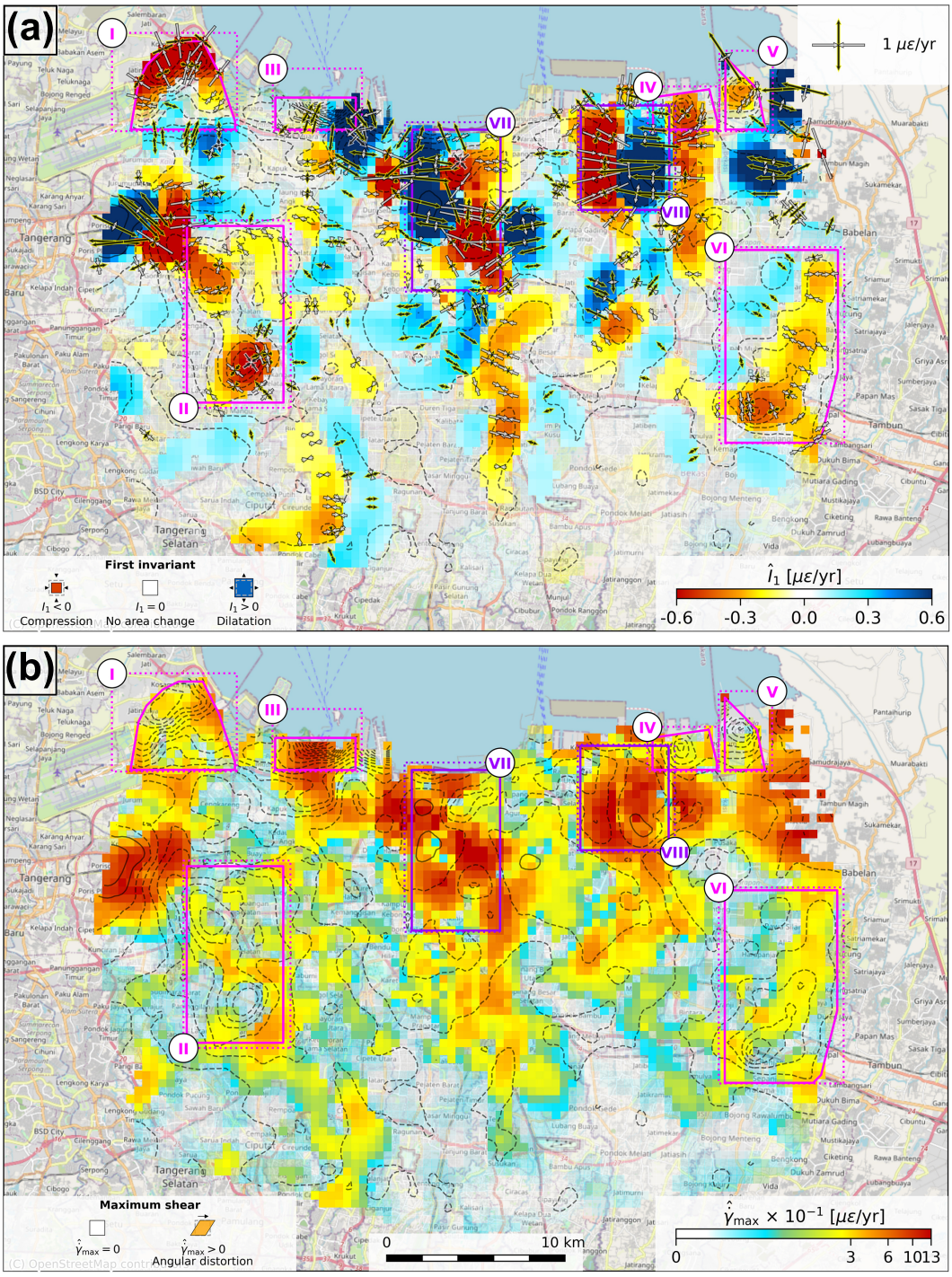


Figure 4. Horizontal strain-rate quantities across Jakarta. Colored cells coincide with the 450×450 m RUMs; only scalar estimates whose magnitudes exceed twice their propagated standard deviation are shown. Magenta outlines mark six major subsidence regions (I–VI), while purple outlines mark regions VII–VIII in Central Jakarta, which exhibit distinct horizontal deformation patterns; the same regions are indicated in the input RUM velocity field in Fig. 3. **(a)** First invariant $\hat{I}_1$, representing horizontal areal contraction ($\hat{I}_1 < 0$) and dilatation ($\hat{I}_1 > 0$). Principal strain-rate glyphs indicate the orientations and relative magnitudes of the maximum and minimum principal strain rates, with black and perpendicular white arrows, respectively. **(b)** Maximum engineering shear strain rate $\widehat{\hat{\gamma}}_{max}$, representing the maximum rate of angular distortion. Regions VII and VIII show pronounced differential deformation.

4.3 Precision and consistency assessment

The propagated uncertainties of $\hat{I}_1$ and $\widehat{\dot{\gamma}}_{\max}$ are lowest in the interior of the finite-element mesh and increase toward its boundaries, where fewer surrounding RUM observations constrain the estimated nodal velocities, see Fig. 5a and b. Approximately 51%

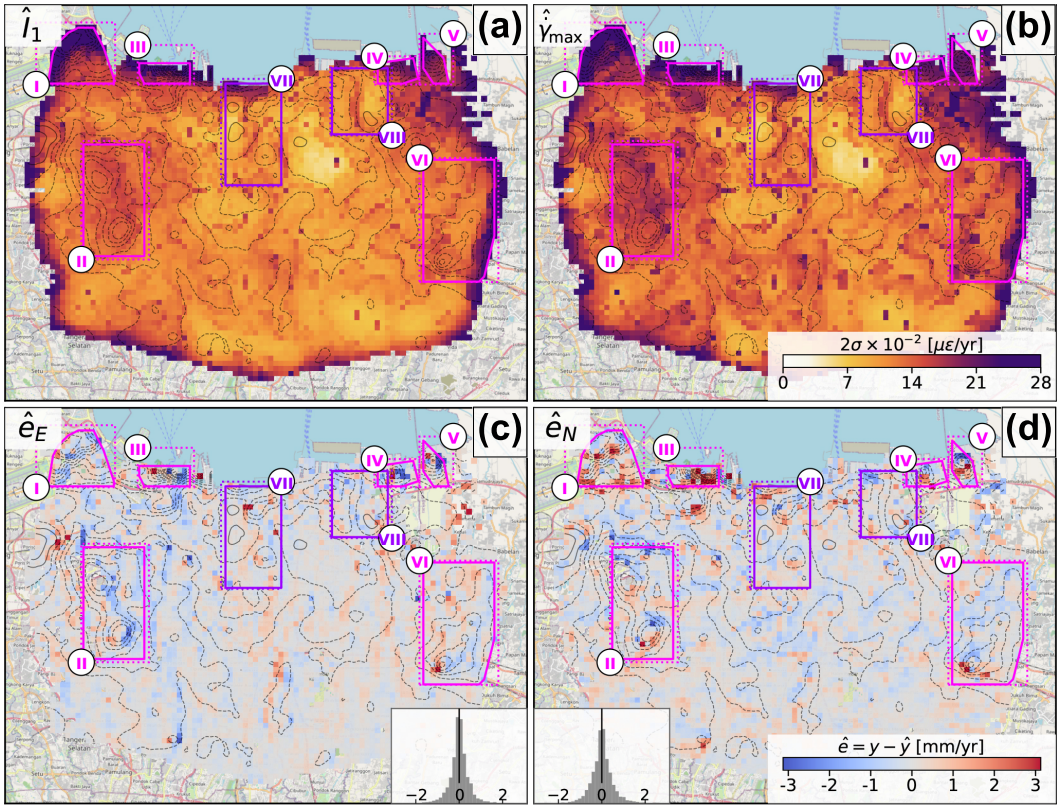


Figure 5. Propagated strain-rate uncertainties and horizontal velocity residuals across Jakarta. Propagated 2σ uncertainties of **(a)** the first invariant, $2\sigma_{I_1}$, and **(b)** the maximum engineering shear strain rate, $2\sigma_{\dot{\gamma}_{\max}}$. **(c,d)** East and north velocity residuals between the observed RUM velocities and their corresponding area-averaged fitted velocities, $\underline{\hat{\mathbf{e}}} = \mathbf{y} - \underline{\hat{\mathbf{y}}}$; inset histograms show their distributions. Magenta outlines mark the six previously identified major subsidence regions (I–VI), and purple outlines regions VII–VIII, as in Fig. 4.

and 55% of the $\hat{I}_1$ and $\widehat{\dot{\gamma}}_{\max}$ estimates, respectively, have magnitudes exceeding twice their propagated standard deviations. These locations therefore show deformation signals that are well resolved relative to their propagated uncertainties.

The residuals between the observed RUM velocities and their corresponding area-averaged fitted velocities are shown in Fig. 5c and d. Their distributions are centered close to zero, with RMS values of 0.57 and 0.67 mm/yr for the east and north components, respectively. These residuals show little systematic spatial structure, indicating that the estimated continuous velocity field reproduces most of the spatial variation in the observed RUM velocities. The clearest exception occurs in the north component within region III, where a spatially coherent residual pattern remains.

5 Discussion

We interpret the horizontal strain-rate patterns derived for Jakarta by comparing them with the vertical and horizontal RUM velocity fields, and discuss the performance, limitations, and applicability of the proposed method.

5.1 Interpretation of the Jakarta deformation

Several of the major subsidence regions in Fig. 4 show a similar horizontal strain-rate pattern, with contraction near the center, large maximum engineering shear strain rates along the flanks, and dilatation farther outward. This pattern is most clearly expressed in the southern part of region II, which we compare with a synthetic axisymmetric subsidence bowl in Fig. 6. The synthetic bowl (Fig. 6a,c) is adapted from empirical settlement models in which vertical displacement follows a Gaussian profile and horizontal displacement follows the gradient of that Gaussian profile (O'Reilly & New, 1982; Mair & Taylor, 1997; Kratzsch, 1983; Franza et al., 2020). For this comparison, the bowl serves as a kinematic reference and is defined by independently prescribed vertical and transversal horizontal velocity fields,

$$v_U(r) = v_U(0)\exp\left(-\frac{r^2}{2\sigma^2}\right), \qquad v_T(r) = v_T(\sigma)\frac{r}{\sigma}\exp\left(\frac{1}{2}-\frac{r^2}{2\sigma^2}\right), \tag{22}$$

where r is the radial distance from the bowl center and σ controls the radial extent of the deformation. Here, $v_U(0)$ is the vertical velocity at the bowl center ($r = 0$), and $v_T(\sigma)$ is the maximum inward transversal velocity at $r = \sigma$. Following the local strapdown coordinate convention for subsidence, U is positive upward, T is radial and positive toward the bowl center, and L is tangential to the iso-displacement contours, with $v_L = 0$. To match the 450×450 m spatial discretization of the strain-rate estimates, the reference horizontal velocity field is sampled on the RUM grid. Per cell, one area-averaged horizontal strain-rate tensor is derived.

The RUM velocity fields and radial profiles for the southern part of region II (Fig. 6b,d,j) show the same center-to-flank variation as the synthetic bowl (Fig. 6a,c,i): vertical subsidence is largest near the center, whereas the horizontal velocity increases toward the flanks. The corresponding synthetic strain-rate maps (Fig. 6e,g) show (i) areal contraction ($I_1 < 0$) near the bowl center, (ii) increasing maximum engineering shear strain rate toward the flanks, and (iii) dilatation ($I_1 > 0$) farther outward.

Because the synthetic horizontal velocity field is axisymmetric, the transversal and longitudinal directions coincide with the principal directions. The radial profiles in Fig. 6k therefore show how the spatial variation of the principal strain rates, $\dot{\varepsilon}_1$ and $\dot{\varepsilon}_2$, determines the *center-to-flank contraction→shear→dilatation* pattern. Near the bowl center, both principal strain rates are negative, resulting in areal contraction ($I_1 < 0$). Toward the bowl's flanks, the transversal principal strain rate $\dot{\varepsilon}_1$ becomes less negative, reaches zero, and then becomes positive, whereas the longitudinal principal strain rate $\dot{\varepsilon}_2$ remains negative. As the difference between the principal strain rates increases toward the flanks, $\dot{\gamma}_{\max}$ increases according to Eq. (8). The maximum $\dot{\gamma}_{\max}$ occurs at the transition between contraction and dilatation ($I_1 = 0$), where $\dot{\varepsilon}_1$ and $\dot{\varepsilon}_2$ have equal magnitudes and opposite signs. Farther outward, transversal extension ($\dot{\varepsilon}_1 > 0$) dominates and I_1 becomes positive, indicating areal dilatation. The corresponding strain-rate maps and radial profiles for the southern part of region II (Fig. 6f,h,l) show the same pattern. Thus, the southern part of region II exhibits the horizontal deformation pattern expected for bowl-shaped subsidence. Similar but less symmetric patterns occur in several other subsidence regions, most clearly in regions IV, V, and the southern part of region VI, see Fig. S1.

The radial extent of the synthetic strain-rate pattern in Fig. 6e,g is controlled by σ in Eq. (22), with larger values extending the deformation over a wider area. Similarly, in simple elastic source models, increasing source depth produces broader surface deformation (Mogi,

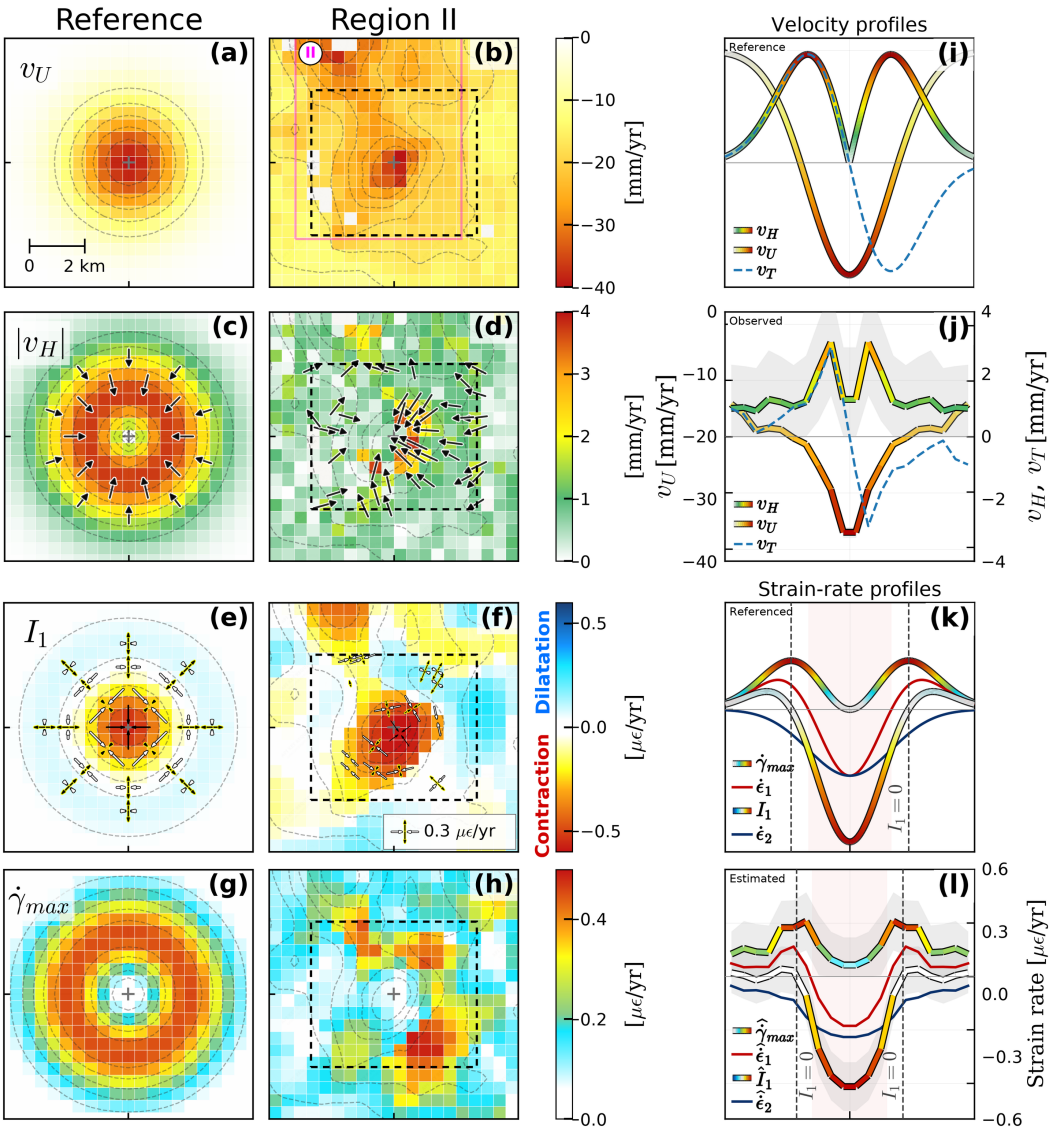


Figure 6. Comparison of the vertical and horizontal velocity fields and derived horizontal strain-rate quantities for a synthetic axisymmetric subsidence bowl (Eq. 22, with $\sigma = 1.5$ km, $v_U(0) = -40.0$ mm/yr, and $v_T(\sigma) = 3.0$ mm/yr) and the southern part of region II in Fig. 4. Panels (a–h) show map views of the synthetic bowl and the southern part of region II: (a,b) vertical velocity v_U; (c,d) horizontal velocity magnitude $|v_H|$, with arrows showing the horizontal velocity direction; (e,f) first invariant I_1 and principal strain-rate glyphs; and (g,h) maximum engineering shear strain rate $\dot{\gamma}_{\max}$. Panels (i–l) compare the corresponding radial profiles of the synthetic bowl and region II: (i,j) v_U, $|v_H|$, and v_T; and (k,l) I_1, $\dot{\gamma}_{\max}$, $\dot{\varepsilon}_1$, and $\dot{\varepsilon}_2$. For region II, the profiles are obtained by grouping cells at similar distances from the bowl center and plotting the median in each distance bin symmetrically about the center. Gray shading in (j,l) shows the 2σ uncertainty ranges of the velocity and strain-rate quantities, respectively. Vertical dashed lines in (k,l) mark $I_1 = 0$, and red shading marks contraction ($I_1 < 0$). The southern part of region II shows the same *center-to-flank contraction→shear→dilatation* pattern as the synthetic bowl.

1958; Geertsma, 1973). Therefore, the relatively wide *contraction→shear→dilatation* patterns identified in regions II, IV, V, and VI are consistent with deep subsidence sources.

By contrast, regions VII and VIII in Central Jakarta contain some of the largest $\widehat{\dot{\gamma}}_{\max}$ values in Jakarta, see Tab. 1, together with localized *non-concentric dilatation–contraction* patterns shown in Fig. 7. Along the transects from A to A', v_T increases to a local maximum near the *dilatation–contraction* transition ($\hat{I}_1 = 0$) and decreases beyond it without reversing direction. Along the same transects, v_U decreases, indicating increasing subsidence toward the contracting side ($\hat{I}_1 < 0$), although the subsidence rates remain smaller than in the major subsidence regions I–VI in Fig. 3. The strong spatial variation in the horizontal motion across these *dilatation–contraction* transitions produces large $\widehat{\dot{\gamma}}_{\max}$. These differential-subsidence patterns may reflect shallower, more localized subsidence sources or lateral transitions between sediment layers compacting at different rates.

To place the estimated horizontal strain rates in region VII in an engineering context, the largest resolved principal strain rate of approximately 1.5 $\mu\varepsilon$/yr is compared with a conservative onset-of-cracking threshold of 200 $\mu\varepsilon$ for masonry buildings (Korff, 2009; Burland et al., 2004; Boone, 2001). If the present ground strain rate were sustained, assuming that strain is accumulating linearly and is being transferred directly to structures, this threshold would be reached after approximately 130 years. This timescale is of the same order as the documented history of subsidence in Jakarta, which extends back to at least 1926 (Schepers, 1926; Schuitenvoerder, 1926). If comparable differential ground deformation has persisted over this period, some structures may already have accumulated strains relevant to the onset of light damage.

5.2 Performance and limitations

The proposed method uses Tikhonov regularization to stabilize the underdetermined estimation of a continuous horizontal velocity field, from area-averaged RUM velocities. The small residuals in Fig. 5c,d. indicate a close fit to the observed RUM velocities, while the comparisons in Figs. 6 and 7 show that the method resolves strain-rate patterns consistent with the observed RUM velocity variations. More than half of the resulting estimated first invariants and maximum engineering shear strain rates exceed twice their propagated standard deviations, see Sec. 4.3. These patterns include bowl-shaped deformation in major subsidence regions, see Fig. 6, and localized *dilatation–contraction* patterns associated with strong horizontal velocity variation, see Fig. 7.

A key advantage is that the method operates directly on strapdown-derived east and north RUM velocities without requiring any additional GNSS velocity constraints. By averaging the interpolated velocity field over each RUM area,the observation model respects the spatial support of the observations while allowing nonlinear velocity variation within individual elements. Furthermore, the RUM velocity covariance information is propagated to the derived strain-rate quantities.

The spatial resolution and precision of the estimated strain-rate field depend on the RUM size, observation coverage, input velocity uncertainties, and regularization. The quadratic finite-element representation accommodates nonlinear velocity variation within elements, but constraining such variation requires sufficient neighboring observations. Consequently, uncertainties increase near mesh boundaries and gaps in RUM coverage (Fig. 5). Regularization introduces an additional trade-off between stability and spatial detail, controlled partly by the neighborhood threshold (d_{thresh}), which should be selected to reflect the spatial scale of the deformation patterns of interest. For Jakarta, the approximately 1770 m variogram range spans almost four RUM widths, indicating spatial coherence across several neighboring RUMs. Guided by this range, we selected $d_{\text{thresh}} = 1350$ m, or three RUM widths, to retain local coupling while limiting smoothing across sharp transitions between deformation regimes. The 450 × 450 m RUM size therefore provides a spatial sampling

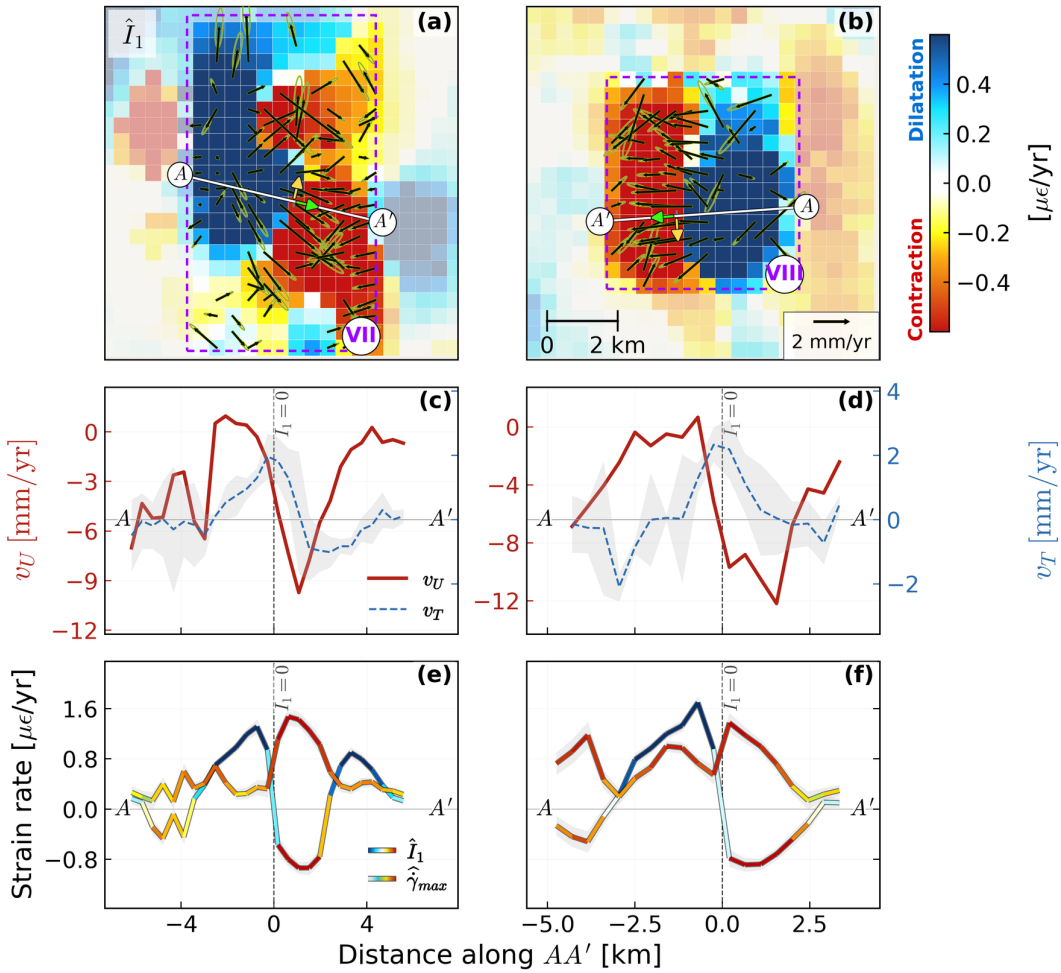


Figure 7. Velocity and strain-rate quantities across the *dilatation–contraction* transitions in regions VII and VIII. Panels (a,b) show the spatial distribution of $\hat{I}_1$ and the horizontal RUM velocity vectors. Transects AA' cross the transition between dilatation ($\hat{I}_1 > 0$) and contraction ($\hat{I}_1 < 0$). Panels (c,d) show the vertical velocity v_U and transversal horizontal velocity v_T along the transects, and panels (e,f) the corresponding profiles of $\hat{I}_1$ and $\hat{\dot{\gamma}}_{\max}$. Gray shading in panels (c–f) denotes the corresponding 2σ uncertainty ranges, and the vertical dashed lines mark the *dilatation–contraction* transitions at $\hat{I}_1 = 0$. In both regions, v_T reaches a local maximum near this transition and decreases beyond it, coinciding with the change in sign of $\hat{I}_1$ and large $\hat{\dot{\gamma}}_{\max}$. Across these transitions, v_U decreases toward the contracting side, although the subsidence rates remain smaller than in the major subsidence regions I–VI. The strong spatial variation in the horizontal motion produces the largest $\hat{\dot{\gamma}}_{\max}$ values in Jakarta.

scale suitable for the city-scale patterns examined here, although finer-scale deformation may remain unresolved.

The method is applicable where the strapdown decomposition provides east and north RUM velocities from multi-track InSAR observations. Its performance depends on the viewing geometry of the available InSAR tracks and on the magnitude and spatial variation of the deformation signal, which control the ability to resolve the horizontal velocity components. The method is particularly relevant for urban areas with limited GNSS coverage, where horizontal strain rates can be estimated without additional GNSS velocity constraints.

6 Conclusions

We developed a method for estimating horizontal strain-rate tensors and derived deformation quantities from strapdown-derived east and north InSAR velocities. The method uses a quadratic finite-element representation with Tikhonov regularization to estimate a continuous horizontal velocity field while explicitly accounting for the area-averaged nature of the RUM observations. The input velocity covariance information is propagated to the derived strain-rate quantities, enabling their precision to be assessed.

Applied to the 2014–2025 velocity field of Jakarta, the method reveals distinct horizontal deformation patterns. Several major subsidence regions exhibit center-to-flank contraction–dilatation patterns consistent with bowl-shaped subsidence originating at greater depth. In Central Jakarta, by contrast, localized non-concentric contraction–dilatation patterns coincide with some of the largest maximum engineering shear strain rates, despite comparatively small vertical subsidence rates. These patterns suggest localized differential deformation, potentially associated with shallower driving mechanisms or lateral variations in sediment compaction. If comparable deformation has persisted since subsidence was first documented in Jakarta in 1926, the accumulated horizontal strains could be relevant to the structural integrity of buildings and infrastructure.

The quadratic finite-element representation accommodates nonlinear horizontal velocity variation over short spatial scales, subject to the constraints imposed by neighboring observations and regularization. By combining this representation with consistent area averaging and uncertainty propagation, the method enables spatially varying horizontal strain rates to be estimated from InSAR observations without requiring additional GNSS velocity constraints, supporting the investigation of localized ground deformation in areas with limited geodetic infrastructure.

Acknowledgments

This work was supported by the Dutch Research Council (NWO) through the Three SISTERS project (grant no. NWO-WOTRO-482.21.505) and by the Merian Fund Southeast Asia–Europe Joint Funding Scheme. Map data © OpenStreetMap contributors (`https://www.openstreetmap.org/copyright`).

Declarations

- **Conflict of interest/Competing interests:** The authors declare there are no conflicts of interest for this manuscript.
- **Author contributions:** A.M.L. designed the research, performed the analysis, created the figures, and wrote the first draft of the manuscript. R.H. reviewed, analyzed, and edited the manuscript.
- **Use of AI tools:** During the preparation of this work, the authors used OpenAI's ChatGPT for proofreading, language editing, improving English writing style, and programming support, including code review, debugging, and implementation assis-

tance. ChatGPT was not used to generate research data, independently perform scientific data analysis, formulate the scientific methodology, or independently derive scientific results, interpretations, or conclusions. All scientific analyses and decisions were carried out and verified by the authors. The authors reviewed and edited all AI-assisted content as needed and take full responsibility for the publication.

Open Research Statement

The input 3D RUM velocity dataset is available from (Lapadat & Hanssen, 2025) (`https://doi.org/10.4121/39e7a39c-d305-425f-b238-1f3a4271dda9`). The horizontal strain-rate fields and associated uncertainty estimates for Jakarta, together with the code implementing the proposed estimation method and reproducing the corresponding figures, are available through 4TU.ResearchData (Lapadat & Hanssen, 2026) (`https://doi.org/10.4121/cff30595-1d98-4e9d-8eb7-0a3000a434fe.v1`).

References

Abidin, H. Z., Andreas, H., Gamal, M., Djaja, R., Subarya, C., Hirose, K., ... Rajiyowiryono, H. (2005). Monitoring Land Subsidence of Jakarta (Indonesia) using Leveling, GPS Survey and InSAR Techniques. In *A Window on the Future of Geodesy: Proceedings of the International Association of Geodesy IAG General Assembly, Sapporo, Japan, june 30–july 11, 2003* (pp. 561–566). doi: 10.1007/3-540-27432-4_95

Anzengruber, S. W., & Ramlau, R. (2010). Morozov's Discrepancy Principle For Tikhonov-Type Functionals With Nonlinear Operators. *Inverse Problems*, *26*(2), 025001. doi: 10.1088/0266-5611/26/2/025001

Aster, R. C., Borchers, B., & Thurber, C. H. (2018). *Parameter Estimation And Inverse Problems*. Elsevier. doi: 10.1016/C2015-0-02458-3

Bathe, K.-J. (1996). *Finite element procedures*. Upper Saddle River, NJ: Prentice Hall.

Boone, R. (2001). Masonry Building Strain Response to Differential Settlement. *Engineering Structures*, *23*, 135–147. doi: 10.1061/40517(295)47

Brouwer, W. S., & Hanssen, R. F. (2023). A Treatise on InSAR Geometry and 3-D Displacement Estimation. *IEEE Transactions on Geoscience and Remote Sensing*, *61*, 1–11. doi: 10.1109/TGRS.2023.3322595

Brouwer, W. S., & Hanssen, R. F. (2024). Estimating Three-Dimensional Displacements with InSAR: The Strapdown Approach. *Journal of Geodesy*, *98*(12), 110. doi: 10.1007/s00190-024-01918-2

Burland, J., Mair, R., & Standing, J. (2004). *Ground performance and building response due to tunnelling*. Emerald Publishing Limited. doi: 10.1680/aigev1.32644.0012

Chaussard, E., Amelung, F., Abidin, H., & Hong, S.-H. (2013). Sinking Cities in Indonesia: ALOS PALSAR detects rapid Subsidence due to Groundwater and Gas Extraction. *Remote Sensing of Environment*, *128*, 150–161. doi: 10.1016/j.rse.2012.10.015

Ding, L., Li, L., Han, W., & Wang, W. (2026). On The Existence Of A Variational Regularization Parameter Under Morozov's Discrepancy Principle For Nonlinear Inverse Problems. *Inverse Problems and Imaging*, *22*, 178–198. doi: 10.3934/ipi.2025049

Elliott, J. R., Fang, J., Lazecký, M., Maghsoudi, Y., Ou, Q., Payne, J. A., ... Wright, T. J. (2026). Deformation, Strains And Velocities For The Alpine Himalayan Belt From Trans-Continental Sentinel-1 InSAR & GNSS. *Remote Sensing of Environment*, *338*, 115320. doi: 10.1016/j.rse.2026.115320

Franza, A., Ritter, S., & DeJong, M. J. (2020). Continuum Solutions For Tunnel–Building Interaction And A Modified Framework For Deformation Prediction. *Géotechnique*, *70*(2), 108–122. doi: 10.1680/jgeot.17.P.279

Geertsma, J. (1973). Land Subsidence Above Compacting Oil And Gas Reservoirs. *Journal of Petroleum Technology*, *25*(06), 734–744. doi: 10.2118/3730-PA

Hanssen, R. F. (2001). *Radar Interferometry: Data Interpretation and Error Analysis*. Springer. doi: 10.1007/0-306-47633-9

Harintaka, H., Suhadha, A. G., Syetiawan, A., Ardha, M., & Rarasati, A. (2024). Current Land Subsidence in Jakarta: A multi-track SBAS InSAR Analysis during 2017–2022 using C-band SAR Data. *Geocarto International*, *39*(1), 2364726. doi: 10.1080/10106049.2024.2364726

Kim, J., Vashishtha, M., Holt, W. E., Murray, K. D., & Lohman, R. B. (2026). A Joint Inversion Algorithm Of GNSS And InSAR For Continuous 3-D Surface Velocities And Associated Horizontal Strain Rate Field. *Geochemistry, Geophysics, Geosystems*, *27*(3), e2025GC012682. doi: 10.1029/2025GC012682

Korff, M. (2009). Deformations and damage to buildings adjacent to deep excavations in soft soils. *Delft Cluster*.

Koudogbo, F. N., Duro, J., Arnaud, A., Bally, P., Abidin, H. Z., & Andreas, H. (2012). Combined X- and L-Band PSI Analyses for Assessment of Land Subsidence in Jakarta. In *Remote Sensing for Agriculture, Ecosystems, and Hydrology xiv* (Vol. 8531, pp. 46–58). doi: 10.1117/12.974821

Kratzsch, H. (1983). *Mining subsidence engineering*. Berlin, Heidelberg: Springer Science & Business Media. doi: 10.1007/978-3-642-81923-0

Kreemer, C., Blewitt, G., & Klein, E. C. (2014). A Geodetic Plate Motion And Global Strain Rate Model. *Geochemistry, Geophysics, Geosystems*, *15*(10), 3849–3889. doi: 10.1002/2014GC005407

Lapadat, A. M., Andreas, H., Brouwer, W., van Diepen, S., Pradipta, D., & Hanssen, R. (2026). Land subsidence in Jakarta in Three Dimensions (2014-2025) using InSAR-GNSS Datum Connection and the strapdown decomposition. *EarthArXiv eprints*, X5R45H. doi: 10.31223/X5R45H

Lapadat, A. M., & Hanssen, R. (2026). *Horizontal strain-rate estimates associated with land subsidence in Jakarta derived from satellite radar interferometry (2014–2025) [Dataset].* 4TU.ResearchData. (Version 1) doi: 10.4121/cff30595-1d98-4e9d-8eb7-0a3000a434fe

Lapadat, A. M., & Hanssen, R. F. (2025). *3D Displacement Velocity Estimates Associated With Groundwater Exploitation In Jakarta Using Satellite Radar Interferometry (2014–2025) [Dataset].* TU Delft – 4TU.ResearchData. doi: 10.4121/39e7a39c-d305-425f-b238-1f3a4271dda9

Mair, R. J., & Taylor, R. N. (1997). Bored Tunnelling In The Urban Environment. In *Proceedings Of The Fourteenth International Conference On Soil Mechanics And Foundation Engineering* (Vol. 4, pp. 2353–2385). A. A. Balkema.

Mogi, K. (1958). Relations Between The Eruptions Of Various Volcanoes And The Deformations Of The Ground Surfaces Around Them. *Bulletin of the Earthquake Research Institute*, *36*(2), 99–134. doi: 10.15083/0000033924

Nair, M. T., Schock, E., & Tautenhahn, U. (2003). Morozov's Discrepancy Principle Under General Source Conditions. *Zeitschrift für Analysis und ihre Anwendungen*, *22*(1), 199–214. doi: 10.4171/ZAA/1140

Ng, A. H.-M., Ge, L., Li, X., Abidin, H. Z., Andreas, H., & Zhang, K. (2012). Mapping Land Subsidence in Jakarta, Indonesia using Persistent Scatterer Interferometry (PSI) Technique with ALOS PALSAR. *International Journal of Applied Earth Observation and Geoinformation*, *18*, 232–242. doi: 10.1016/j.jag.2012.01.018

Nozue, Y., & Fukahata, Y. (2025). Geodetic Data Inversion To Estimate A Strain-Rate Field By Introducing Sparse Modeling. *Earth, Planets and Space*, *77*(1), 12. doi: 10.1186/s40623-024-02115-3

Okazaki, T., Fukahata, Y., & Nishimura, T. (2021). Consistent Estimation Of Strain-Rate Fields From GNSS Velocity Data Using Basis Function Expansion With ABIC. *Earth, Planets and Space*, *73*(1), 153. doi: 10.1186/s40623-021-01474-5

O'Reilly, M. P., & New, B. M. (1982). Settlements Above Tunnels In The United Kingdom–Their Magnitude And Prediction. In *Tunnelling '82: Proceedings Of The Third International Symposium* (pp. 173–181). Institution of Mining and Metallurgy.

Ou, Q., Daout, S., Weiss, J. R., Shen, L., Lazecký, M., Wright, T. J., & Parsons, B. E. (2022). Large-Scale Interseismic Strain Mapping Of The NE Tibetan Plateau From

Sentinel-1 Interferometry. *Journal of Geophysical Research: Solid Earth*, *127*(6), e2022JB024176. doi: 10.1029/2022JB024176

Pagli, C., Wang, H., Wright, T. J., Calais, E., & Lewi, E. (2014). Current Plate Boundary Deformation Of The Afar Rift From A 3-D Velocity Field Inversion Of InSAR And GPS. *Journal of Geophysical Research: Solid Earth*, *119*(11), 8562–8575. doi: 10.1002/2014JB011391

Savage, J. C., & Burford, R. O. (1970). Accumulation Of Tectonic Strain In California. *Bulletin of the Seismological Society of America*, *60*(6), 1877–1896. doi: 10.1785/BSSA0600061877

Savage, J. C., Gan, W., & Svarc, J. L. (2001). Strain Accumulation and Rotation in the Eastern California Shear Zone. *Journal of Geophysical Research: Solid Earth*, *106*(B10), 21995-22007. doi: 10.1029/2000JB000127

Schepers, J. (1926). De Nauwkeurigheidswaterpassing van Java, de Primaire Kringen 1a en ii, benevens het Stadsnet van Batavia en Weltevreden. *Verhandelingen No. 1, Topografische Dienst in Nederlandsch-Indië*.

Schuitenvoerder, H. (1926). De Nauwkeurigheidswaterpassing van Java. *Jaarverslag van den Topografischen Dienst in Nederlandsch-Indië*, *1925*.

Shen, Z.-K., Jackson, D. D., & Ge, B. X. (1996). Crustal Deformation Across And Beyond The Los Angeles Basin From Geodetic Measurements. *Journal of Geophysical Research: Solid Earth*, *101*(B12), 27957–27980. doi: 10.1029/96JB02544

Shen, Z.-K., Wang, M., Zeng, Y., & Wang, F. (2015). Optimal Interpolation Of Spatially Discretized Geodetic Data. *Bulletin of the Seismological Society of America*, *105*(4), 2117–2127. doi: 10.1785/0120140247

Sidiq, T. P., Gumilar, I., Abidin, H. Z., Meilano, I., Purwarianti, A., & Lestari, R. (2025). Spatial Distribution and Monitoring of Land Subsidence using Sentinel-1 SAR Data in Java, Indonesia. *Applied Sciences*, *15*(7). doi: 10.3390/app15073732

Tape, C., Musé, P., Simons, M., Dong, D., & Webb, F. (2009). Multiscale Estimation Of GPS Velocity Fields. *Geophysical Journal International*, *179*(2), 945–971. doi: 10.1111/j.1365-246X.2009.04337.x

Tarantola, A. (2005). *Inverse Problem Theory And Methods For Model Parameter Estimation*. SIAM. doi: 10.1137/1.9780898717921

Tymofyeyeva, E., & Fialko, Y. (2018). Geodetic Evidence For A Blind Fault Segment At The Southern End Of The San Jacinto Fault Zone. *Journal of Geophysical Research: Solid Earth*, *123*(1), 878–891. doi: 10.1002/2017JB014477

UN. (2025, November). *World urbanization prospects 2025: Summary of results* (Tech. Rep. No. UN DESA/POP/2025/TR/NO. 12). New York: United Nations, Department of Economic and Social Affairs, Population Division. Retrieved from `https://population.un.org/wup/assets/Publications/undesa_pd_2025_wup2025_summary_of_results_final.pdf`

Walters, R. J., Parsons, B., & Wright, T. J. (2014). Constraining Crustal Velocity Fields With InSAR For Eastern Turkey: Limits To The Block-Like Behavior Of Eastern Anatolia. *Journal of Geophysical Research: Solid Earth*, *119*, 5215–5234. doi: 10.1002/2013JB010909

Wang, H., Wright, T. J., Liu-Zeng, J., & Peng, L. (2019). Strain Rate Distribution In South-Central Tibet From Two Decades Of InSAR And GPS. *Geophysical Research Letters*, *46*(10), 5170–5179. doi: 10.1029/2019GL081916

Weiss, J. R., Walters, R. J., Morishita, Y., Wright, T. J., Lazecky, M., Wang, H., ... Parsons, B. (2020). High-Resolution Surface Velocities And Strain For Anatolia From Sentinel-1 InSAR And GNSS Data. *Geophysical Research Letters*, *47*(17), e2020GL087376. doi: 10.1029/2020GL087376

Welsch, W. M. (1986). Some Aspects Of The Analysis Of Geodetic Strain Observations In Kinematic Models. *Tectonophysics*, *130*(1–4), 437–458. doi: 10.1016/0040-1951(86)90132-0

Widodo, J., Herlambang, A., Sulaiman, A., Razi, P., Perissin, D., Kuze, H., & Sumantyo, J. T. S. (2019). Land Subsidence Rate Analysis of Jakarta Metropolitan Region based

on D-InSAR Processing of Sentinel Data C-band Frequency. In *Journal of Physics: Conference Series* (Vol. 1185, p. 012004). doi: 10.1088/1742-6596/1185/1/012004

Wright, T. J., Parsons, B. E., & Lu, Z. (2004). Toward Mapping Surface Deformation In Three Dimensions Using InSAR. *Geophysical Research Letters*, *31*(1). doi: 10.1029/2003GL018827

Xu, X., Sandwell, D. T., Klein, E., & Bock, Y. (2021). Integrated Sentinel-1 InSAR And GNSS Time-Series Along The San Andreas Fault System. *Journal of Geophysical Research: Solid Earth*, *126*(11), e2021JB022579. doi: 10.1029/2021JB022579

Supporting Information for "Horizontal Strain Rate estimation from InSAR Observations and the Strapdown Method"

Alexandru M. Lapadat[1], Ramon F. Hanssen[1]

[1]Mathematical Geodesy and Positioning, Delft University of Technology, Stevinweg 1, Delft, Netherlands

Contents of this file

1. Text S1. Finite-element operators, regularization, and uncertainty propagation.
2. Text S2. Additional horizontal strain-rate maps.
3. Figure S1. Close-up of the Jakarta strain-rate maps.

S1. Finite-element operators, regularization, and uncertainty propagation

This supplementary section provides the mathematical and implementation details of the methodology introduced in Sec. 3. Specifically, it gives the explicit construction of the observation matrix $\mathbf{A}$, the strain-rate mapping matrix $\mathbf{B}$, and the regularization operator $\mathbf{L}$, and details the propagation of the RUM velocity uncertainties to the derived strain-rate quantities $(\hat{I}_1, \widehat{\dot{\gamma}}_{\max}, \hat{\dot{\varepsilon}}_{1,2})$.

The input consists of the area-averaged east and north velocity observations for Regions of Uniform Motion (RUMs) and their variance–covariance information, while the east and north velocities at the finite-element nodes are the estimation unknowns. The four subsections below detail the finite-element representation and Q8 interpolation, the observation

model and construction of the observation matrix, the strain-rate mapping and regularization operators, and uncertainty propagation to the derived strain-rate quantities.

S1.1. Finite-element representation and Q8 interpolation

The horizontal velocity field is represented by a mesh of eight-node quadratic quadrilateral (Q8) finite elements. Each observed RUM coincides with one finite element of the same spatial extent, while elements without RUM observations are retained to maintain connectivity of the finite-element mesh. The east and north velocity components at the mesh nodes are the estimation unknowns. Adjacent finite elements share their boundary nodes and, consequently, the corresponding nodal velocity unknowns.

Each finite element e has eight nodes, indexed by $a = 1, \ldots, 8$. Within the element, the horizontal velocity field is obtained by quadratic interpolation of the nodal velocities,

$$\mathbf{v}_e(\xi, \eta) = \sum_{a=1}^{8} N_a(\xi, \eta)\, \mathbf{v}_a, \tag{S1}$$

where $(\xi, \eta) \in [-1, 1] \times [-1, 1]$ are the local element coordinates, $N_a(\xi, \eta)$ is the quadratic shape function associated with node a, and $\mathbf{v}_a = [v_{\mathrm{E},a}, v_{\mathrm{N},a}]^T$ contains the unknown east and north velocity components at that node.

For the adopted node ordering, nodes 1–4 are the southwest, southeast, northeast, and northwest corner nodes, respectively, while nodes 5–8 are the south, east, north, and west midside nodes. The corresponding quadratic interpolation functions are

$$N_1 = -\tfrac{1}{4}(1-\xi)(1-\eta)(1+\xi+\eta), \qquad N_2 = -\tfrac{1}{4}(1+\xi)(1-\eta)(1-\xi+\eta), \tag{S2}$$

$$N_3 = -\tfrac{1}{4}(1+\xi)(1+\eta)(1-\xi-\eta), \qquad N_4 = -\tfrac{1}{4}(1-\xi)(1+\eta)(1+\xi-\eta), \tag{S3}$$

$$N_5 = \tfrac{1}{2}(1-\xi^2)(1-\eta), \qquad N_6 = \tfrac{1}{2}(1+\xi)(1-\eta^2), \tag{S4}$$

$$N_7 = \tfrac{1}{2}(1-\xi^2)(1+\eta), \qquad N_8 = \tfrac{1}{2}(1-\xi)(1-\eta^2). \tag{S5}$$

Because adjacent elements share their boundary nodes and corresponding nodal velocity unknowns, Eq. (S1) defines a continuous horizontal velocity field across the finite-element mesh.

S1.2. Observation model and construction of the observation matrix

To relate the nodal velocity field to the area-averaged RUM observations, the observation matrix $\mathbf{A}$ is constructed from area-averaged quadratic shape functions. Because each observed RUM velocity represents the average horizontal motion over its area, the corresponding prediction is obtained by averaging the interpolated velocity field over the same area. This ensures that the predicted and observed RUM velocities have the same spatial support.

For each observed RUM i, element e denotes the corresponding finite element with the same spatial extent. Averaging Eq. (S1) over this element gives

$$\frac{1}{|\Omega_e|}\int_{\Omega_e} \mathbf{v}_e(\xi,\eta)\,\mathrm{d}\Omega = \sum_{a=1}^{8} \bar{N}_{a,e}\mathbf{v}_a, \qquad \bar{N}_{a,e} = \frac{1}{|\Omega_e|}\int_{\Omega_e} N_a(\xi,\eta)\,\mathrm{d}\Omega, \tag{S6}$$

where Ω_e denotes the domain of element e, $|\Omega_e|$ its area, and $\bar{N}_{a,e}$ the area average of shape function N_a over the element.

The integral defining $\bar{N}_{a,e}$ is evaluated numerically using 3×3 Gauss quadrature. The local element coordinates (ξ, η) are related to the physical east-north coordinates (E, N) through the Jacobian

$$\mathbf{J}_e = \begin{bmatrix} \partial \mathrm{E}/\partial\xi & \partial \mathrm{E}/\partial\eta \\ \partial \mathrm{N}/\partial\xi & \partial \mathrm{N}/\partial\eta \end{bmatrix}, \tag{S7}$$

whose absolute determinant converts an area element in local coordinates to physical area. Using the three Gauss points $(-\sqrt{3/5}, 0, \sqrt{3/5})$ with corresponding quadrature weights

$(5/9, 8/9, 5/9)$ in each coordinate direction, gives

$$\bar{N}_{a,e} \approx \frac{1}{|\Omega_e|} \sum_{p=1}^{3} \sum_{q=1}^{3} w_p w_q \, N_a(\xi_p, \eta_q) \; |\det \mathbf{J}_e(\xi_p, \eta_q)| \, . \tag{S8}$$

The area-averaged shape functions $\bar{N}_{a,e}$ form the nonzero entries of the observation matrix $\mathbf{A}$. Denoting the mesh-wide index of local node a of element e by $j_e(a)$, the row corresponding to RUM i contains

$$(\mathbf{A}_{\mathrm{E}})_{i,j_e(a)} = (\mathbf{A}_{\mathrm{N}})_{i,j_e(a)} = \bar{N}_{a,e}, \qquad a = 1, \ldots, 8, \tag{S9}$$

for both the east and north observation-matrix blocks, with all remaining entries in that row equal to zero.

Stacking the observed RUM velocity components in $\underline{\mathbf{y}}$, with all east components followed by all north components, and arranging the nodal velocity unknowns in $\mathbf{x}$ in the same order, gives the observation model

$$\underline{\mathbf{y}} = \mathbf{A}\mathbf{x} + \underline{\boldsymbol{\eta}}, \qquad \mathbf{A} = \begin{bmatrix} \mathbf{A}_{\mathrm{E}} & \mathbf{0} \\ \mathbf{0} & \mathbf{A}_{\mathrm{N}} \end{bmatrix}, \tag{S10}$$

where $\mathbf{A}$ maps the nodal velocity unknowns to the predicted area-averaged RUM velocities, and $\underline{\boldsymbol{\eta}}$ contains the RUM velocity observation errors.

The observation errors are assumed to have zero mean and variance–covariance matrix $\mathbf{Q}_{yy}$. This matrix retains the east–north covariance within each RUM and assumes zero covariance between different RUMs (Brouwer & Hanssen, 2023, 2024). The corresponding weight matrix used in the regularized estimation is $\mathbf{W} = \mathbf{Q}_{yy}^{-1}$.

S1.3. Construction of the strain-rate mapping and regularization operators

The regularization operator $\mathbf{L}$ combines two terms. The first, $\mathbf{L}_v$, penalizes spatial variations in gradients of the horizontal velocity field. The second, $\mathbf{L}_{\dot{\varepsilon}\to x}$, penalizes large differences in element-averaged horizontal strain-rate tensors between neighboring finite

elements. Because the estimation unknowns are the nodal velocities, construction of the second term requires a mapping from the nodal velocities to the element-averaged strain-rate components. We therefore first construct this mapping, represented by $\mathbf{B}$.

For finite element e, the three independent components of the horizontal strain-rate tensor are $\dot{\varepsilon}_{\mathrm{EE},e}$, $\dot{\varepsilon}_{\mathrm{NN},e}$, and $\dot{\varepsilon}_{\mathrm{EN},e}$, with $\dot{\varepsilon}_{\mathrm{EE}} = \partial v_{\mathrm{E}}/\partial \mathrm{E}$, $\dot{\varepsilon}_{\mathrm{NN}} = \partial v_{\mathrm{N}}/\partial \mathrm{N}$, and $\dot{\varepsilon}_{\mathrm{EN}} = \frac{1}{2}(\partial v_{\mathrm{E}}/\partial \mathrm{N} + \partial v_{\mathrm{N}}/\partial \mathrm{E})$. These components are obtained by differentiating the quadratic interpolation in Eq. (S1). Since the interpolation functions N_a are defined in the local element coordinates (ξ, η), their derivatives are transformed to the physical east–north coordinates (E, N) using

$$\begin{bmatrix} \partial N_a/\partial \mathrm{E} \\ \partial N_a/\partial \mathrm{N} \end{bmatrix} = \mathbf{J}_e^{-T} \begin{bmatrix} \partial N_a/\partial \xi \\ \partial N_a/\partial \eta \end{bmatrix}, \tag{S11}$$

where $\mathbf{J}_e$ is the Jacobian defined in Eq. (S7).

The methodology in Sec. 3 derives one element-averaged horizontal strain-rate tensor for each finite element. The transformed derivatives are therefore averaged over the element using the same 3×3 Gauss quadrature as in Eq. (S8). Here, $\overline{\partial N_a/\partial \mathrm{E}}$ and $\overline{\partial N_a/\partial \mathrm{N}}$ denote these element-averaged derivatives.

Let $\mathbf{x}_e \in \mathbb{R}^{16}$ contain the eight east nodal velocities followed by the eight north nodal velocities of element e. The three element-averaged strain-rate components are then obtained from

$$[\dot{\varepsilon}_{\mathrm{EE},e}\ \dot{\varepsilon}_{\mathrm{NN},e}\ \dot{\varepsilon}_{\mathrm{EN},e}]^T = \mathbf{B}_e \mathbf{x}_e, \qquad \mathbf{B}_e = \begin{bmatrix} \overline{\frac{\partial N_1}{\partial \mathrm{E}}} & \cdots & \overline{\frac{\partial N_8}{\partial \mathrm{E}}} & 0 & \cdots & 0 \\ 0 & \cdots & 0 & \overline{\frac{\partial N_1}{\partial \mathrm{N}}} & \cdots & \overline{\frac{\partial N_8}{\partial \mathrm{N}}} \\ \frac{1}{2}\overline{\frac{\partial N_1}{\partial \mathrm{N}}} & \cdots & \frac{1}{2}\overline{\frac{\partial N_8}{\partial \mathrm{N}}} & \frac{1}{2}\overline{\frac{\partial N_1}{\partial \mathrm{E}}} & \cdots & \frac{1}{2}\overline{\frac{\partial N_8}{\partial \mathrm{E}}} \end{bmatrix}. \tag{S12}$$

Assembling the element matrices $\mathbf{B}_e$ over the finite-element mesh gives $\mathbf{B} \in \mathbb{R}^{3n_e \times 2n_n}$, where n_e and n_n denote the total numbers of finite elements and distinct mesh nodes,

respectively. This matrix maps the nodal velocities to the three element-averaged strain-rate components of every finite element.

We next construct the velocity regularization term $\mathbf{L}_v$. For one velocity component, the spatial derivatives of the quadratic interpolation functions are collected at each Gauss point in

$$\mathbf{G}_e = \begin{bmatrix} \partial_{\mathrm{E}} N_1 & \cdots & \partial_{\mathrm{E}} N_8 \\ \partial_{\mathrm{N}} N_1 & \cdots & \partial_{\mathrm{N}} N_8 \\ \partial_{\mathrm{E}} N_1 & \cdots & \partial_{\mathrm{E}} N_8 \\ \partial_{\mathrm{N}} N_1 & \cdots & \partial_{\mathrm{N}} N_8 \\ \frac{1}{2}(\partial_{\mathrm{E}} N_1 + \partial_{\mathrm{N}} N_1) & \cdots & \frac{1}{2}(\partial_{\mathrm{E}} N_8 + \partial_{\mathrm{N}} N_8) \\ \frac{1}{2}(\partial_{\mathrm{E}} N_1 + \partial_{\mathrm{N}} N_1) & \cdots & \frac{1}{2}(\partial_{\mathrm{E}} N_8 + \partial_{\mathrm{N}} N_8) \end{bmatrix} \in \mathbb{R}^{6\times 8}, \tag{S13}$$

where $\partial_{\mathrm{E}} N_a$ and $\partial_{\mathrm{N}} N_a$ denote the physical-coordinate derivatives from Eq. (S11). The corresponding element contribution to the velocity regularization term is

$$\mathbf{L}_{v,e} \approx \sum_{p=1}^{3}\sum_{q=1}^{3} w_p w_q \, \mathbf{G}_e(\xi_p, \eta_q)^T \mathbf{G}_e(\xi_p, \eta_q) \, \left|\det \mathbf{J}_e(\xi_p, \eta_q)\right| . \tag{S14}$$

The element contributions $\mathbf{L}_{v,e}$ are assembled over the finite-element mesh to form the velocity regularization term for one velocity component. Applying the same term to the east and north nodal velocities gives $\mathbf{L}_v = \mathrm{blkdiag}(\mathbf{L}_{v_{\mathrm{E}}}, \mathbf{L}_{v_{\mathrm{N}}})$, and the associated regularization penalty is $\|\mathbf{L}_v \mathbf{x}\|_2^2$.

The second regularization term $\mathbf{L}_{\dot{\varepsilon}\to x}$ penalizes differences between the horizontal strain-rate tensors of neighboring finite elements. Rather than coupling all neighboring elements equally, the coupling is stronger for elements that are spatially close and have similar deformation. Because the estimated strain-rate field is not yet available when the regularization is constructed, deformation similarity is approximated from proxy strain-rate tensors obtained by fitting planar horizontal velocity fields to nearby observed RUM velocities. For each finite element e, the planar horizontal velocity field

$$v_{\mathrm{E}}(\mathrm{E},\mathrm{N}) = \beta_0 + \beta_1 \mathrm{E} + \beta_2 \mathrm{N}, \qquad v_{\mathrm{N}}(\mathrm{E},\mathrm{N}) = \gamma_0 + \gamma_1 \mathrm{E} + \gamma_2 \mathrm{N} \tag{S15}$$

is fitted by ordinary least squares to the observed RUM velocities whose centers lie within d_{thresh} of the element centroid. The symmetric part of the fitted velocity gradient tensor gives the proxy strain-rate tensor,

$$\begin{bmatrix} \tilde{\dot{\varepsilon}}_{\text{EE},e} & \tilde{\dot{\varepsilon}}_{\text{EN},e} \\ \tilde{\dot{\varepsilon}}_{\text{EN},e} & \tilde{\dot{\varepsilon}}_{\text{NN},e} \end{bmatrix} = \begin{bmatrix} \beta_1 & \frac{1}{2}(\beta_2 + \gamma_1) \\ \frac{1}{2}(\beta_2 + \gamma_1) & \gamma_2 \end{bmatrix}. \tag{S16}$$

Its two eigenvalues, $\tilde{\boldsymbol{\lambda}}_e = [\tilde{\dot{\varepsilon}}_{1,e} \ \tilde{\dot{\varepsilon}}_{2,e}]^T$, are the proxy principal strain rates. These proxy quantities are used only to determine the regularization weights and are not estimation unknowns.

For element e, let $\mathcal{N}_e = \{k : d_{ek} \leq d_{\text{thresh}}\}$ denote its neighboring elements, where d_{ek} is the centroid-to-centroid distance between elements e and k. For each neighboring pair, $\Delta\lambda_{ek} = \|\tilde{\boldsymbol{\lambda}}_e - \tilde{\boldsymbol{\lambda}}_k\|_2$ denotes the Euclidean distance between their proxy principal strain-rate vectors, indicating how much their local deformation states differ.

The coupling weight for each neighboring pair is

$$w_{ek} = w_{\text{dist}}\, w_{\dot{\varepsilon}}, \qquad w_{\text{dist}} = \frac{1}{1 + (d_{ek}/d_{\text{thresh}})^2}, \qquad w_{\dot{\varepsilon}} = \exp\!\left(-\frac{\Delta\lambda_{ek}^2}{\sigma_{\dot{\varepsilon}}^2}\right), \tag{S17}$$

where $\sigma_{\dot{\varepsilon}}$ is estimated from the median absolute deviation of $\Delta\lambda_{ek}$ over the neighboring element pairs. Thus, w_{ek} decreases with increasing spatial separation or increasing differences between the proxy principal strain-rate vectors.

These weights define the strain-rate regularization matrix $\mathbf{L}_{\dot{\varepsilon}}$. For each element, this matrix forms the weighted differences between its three strain-rate tensor components and those of its neighboring elements. The contribution associated with element e is

$$\sum_{k \in \mathcal{N}_e} w_{ek} \left(\begin{bmatrix} \dot{\varepsilon}_{\text{EE},e} \\ \dot{\varepsilon}_{\text{NN},e} \\ \dot{\varepsilon}_{\text{EN},e} \end{bmatrix} - \begin{bmatrix} \dot{\varepsilon}_{\text{EE},k} \\ \dot{\varepsilon}_{\text{NN},k} \\ \dot{\varepsilon}_{\text{EN},k} \end{bmatrix} \right). \tag{S18}$$

Because these strain-rate components are obtained from the nodal velocities through $\mathbf{B}$, the strain-rate regularization matrix is mapped to nodal-velocity space as

$$\mathbf{L}_{\dot{\varepsilon}\to x} = \mathbf{L}_{\dot{\varepsilon}}\mathbf{B}. \tag{S19}$$

Before the two regularization terms are combined, they are normalized so that their relative influence is not determined by differences in numerical scale. The velocity regularization term $\mathbf{L}_v$ and the strain-rate regularization matrix $\mathbf{L}_{\dot{\varepsilon}}$ are first normalized by their mean absolute row sums. After mapping $\mathbf{L}_{\dot{\varepsilon}}$ to nodal-velocity space, the three strain-rate component groups of $\mathbf{L}_{\dot{\varepsilon}\to x}$ are rescaled to the Frobenius norm of $\mathbf{L}_v$. The final regularization operator is

$$\mathbf{L} = \begin{bmatrix} \mathbf{L}_v \\ \mathbf{L}_{\dot{\varepsilon}\to x} \end{bmatrix}. \tag{S20}$$

With the observation matrix $\mathbf{A}$, weight matrix $\mathbf{W}$, and regularization operator $\mathbf{L}$ defined, the nodal velocities are estimated using weighted Tikhonov regularization, with the regularization parameter α selected using the Morozov discrepancy principle, as described in Sec. 3 (Eqs. (15)–(17)).

S1.4. Uncertainty propagation to the strain-rate quantities

The uncertainty propagation starts from the variance–covariance matrix $\mathbf{Q}_{yy}$ of the observed east and north RUM velocities, whose inverse defines the weight matrix $\mathbf{W} = \mathbf{Q}_{yy}^{-1}$ in Eq. (S1.2). The RUM velocity uncertainties are first propagated through the regularized estimation to the estimated nodal velocities, then through the strain-rate mapping $\mathbf{B}$ to the element-averaged strain-rate components, and finally to the computed strain-rate quantities $\hat{I}_1$, $\widehat{\dot{\gamma}}_{\max}$, and $\hat{\dot{\varepsilon}}_{1,2}$by first-order Taylor linearization.

Treating the selected regularization parameter α and regularization operator $\mathbf{L}$ as fixed, the variance–covariance matrix of the estimated nodal velocities is

$$\mathbf{Q}_{\hat{x}} = \left(\mathbf{A}^T\mathbf{W}\mathbf{A} + \alpha^2\mathbf{L}^T\mathbf{L}\right)^{-1}\mathbf{A}^T\mathbf{W}\mathbf{A}\left(\mathbf{A}^T\mathbf{W}\mathbf{A} + \alpha^2\mathbf{L}^T\mathbf{L}\right)^{-1}. \tag{S21}$$

The three element-averaged strain-rate components are obtained from the estimated nodal velocities through the linear mapping $\mathbf{B}$. Their variance–covariance matrix is therefore

$$\mathbf{Q}_{\hat{\dot{\varepsilon}}} = \mathbf{B}\mathbf{Q}_{\hat{x}}\mathbf{B}^T. \tag{S22}$$

For finite element e, $\mathbf{Q}_{\hat{\dot{\varepsilon}},e}$ denotes the corresponding 3×3 diagonal block of $\mathbf{Q}_{\hat{\dot{\varepsilon}}}$ and contains the variances and covariances of $[\hat{\dot{\varepsilon}}_{\mathrm{EE},e}\ \hat{\dot{\varepsilon}}_{\mathrm{NN},e}\ \hat{\dot{\varepsilon}}_{\mathrm{EN},e}]^T$.

The uncertainties of the computed strain-rate quantities are propagated from $\mathbf{Q}_{\hat{\dot{\varepsilon}},e}$ using first-order Taylor linearization. For a strain-rate quantity f, this gives

$$\sigma^2_{f,e} \approx \mathbf{J}_{f,e}\mathbf{Q}_{\hat{\dot{\varepsilon}},e}\mathbf{J}^T_{f,e}, \tag{S23}$$

where $\mathbf{J}_{f,e}$ is the Jacobian of f with respect to $[\dot{\varepsilon}_{\mathrm{EE},e}\ \dot{\varepsilon}_{\mathrm{NN},e}\ \dot{\varepsilon}_{\mathrm{EN},e}]^T$, evaluated at the estimated strain-rate components of element e.

For the first invariant, $\hat{I}_{1,e} = \hat{\dot{\varepsilon}}_{\mathrm{EE},e} + \hat{\dot{\varepsilon}}_{\mathrm{NN},e}$, and therefore $\mathbf{J}_{I_1} = [1\ 1\ 0]$. For the nonlinear quantities, define $d_e = \hat{\dot{\varepsilon}}_{\mathrm{EE},e} - \hat{\dot{\varepsilon}}_{\mathrm{NN},e}$ and $\Delta_e = \sqrt{d_e^2 + 4\hat{\dot{\varepsilon}}^2_{\mathrm{EN},e}}$. Then $\hat{\dot{\gamma}}_{\max,e} = \Delta_e$ and $\hat{\dot{\varepsilon}}_{1,2,e} = \frac{1}{2}[\hat{\dot{\varepsilon}}_{\mathrm{EE},e} + \hat{\dot{\varepsilon}}_{\mathrm{NN},e} \pm \Delta_e]$. The corresponding Jacobians are

$$\mathbf{J}_{\dot{\gamma}_{\max},e} = \left[\frac{d_e}{\Delta_e}\ \ -\frac{d_e}{\Delta_e}\ \ \frac{4\hat{\dot{\varepsilon}}_{\mathrm{EN},e}}{\Delta_e}\right], \tag{S24}$$

$$\mathbf{J}_{\dot{\varepsilon}_1,e} = \left[\frac{1}{2}\left(1+\frac{d_e}{\Delta_e}\right)\ \ \frac{1}{2}\left(1-\frac{d_e}{\Delta_e}\right)\ \ \frac{2\hat{\dot{\varepsilon}}_{\mathrm{EN},e}}{\Delta_e}\right], \tag{S25}$$

$$\mathbf{J}_{\dot{\varepsilon}_2,e} = \left[\frac{1}{2}\left(1-\frac{d_e}{\Delta_e}\right)\ \ \frac{1}{2}\left(1+\frac{d_e}{\Delta_e}\right)\ \ -\frac{2\hat{\dot{\varepsilon}}_{\mathrm{EN},e}}{\Delta_e}\right]. \tag{S26}$$

Substituting these Jacobians into Eq. (S23) gives the propagated standard deviations of $\hat{I}_1$, $\widehat{\dot{\gamma}}_{\max}$, and $\hat{\dot{\varepsilon}}_{1,2}$.

S2. Additional Horizontal Strain-rate Maps

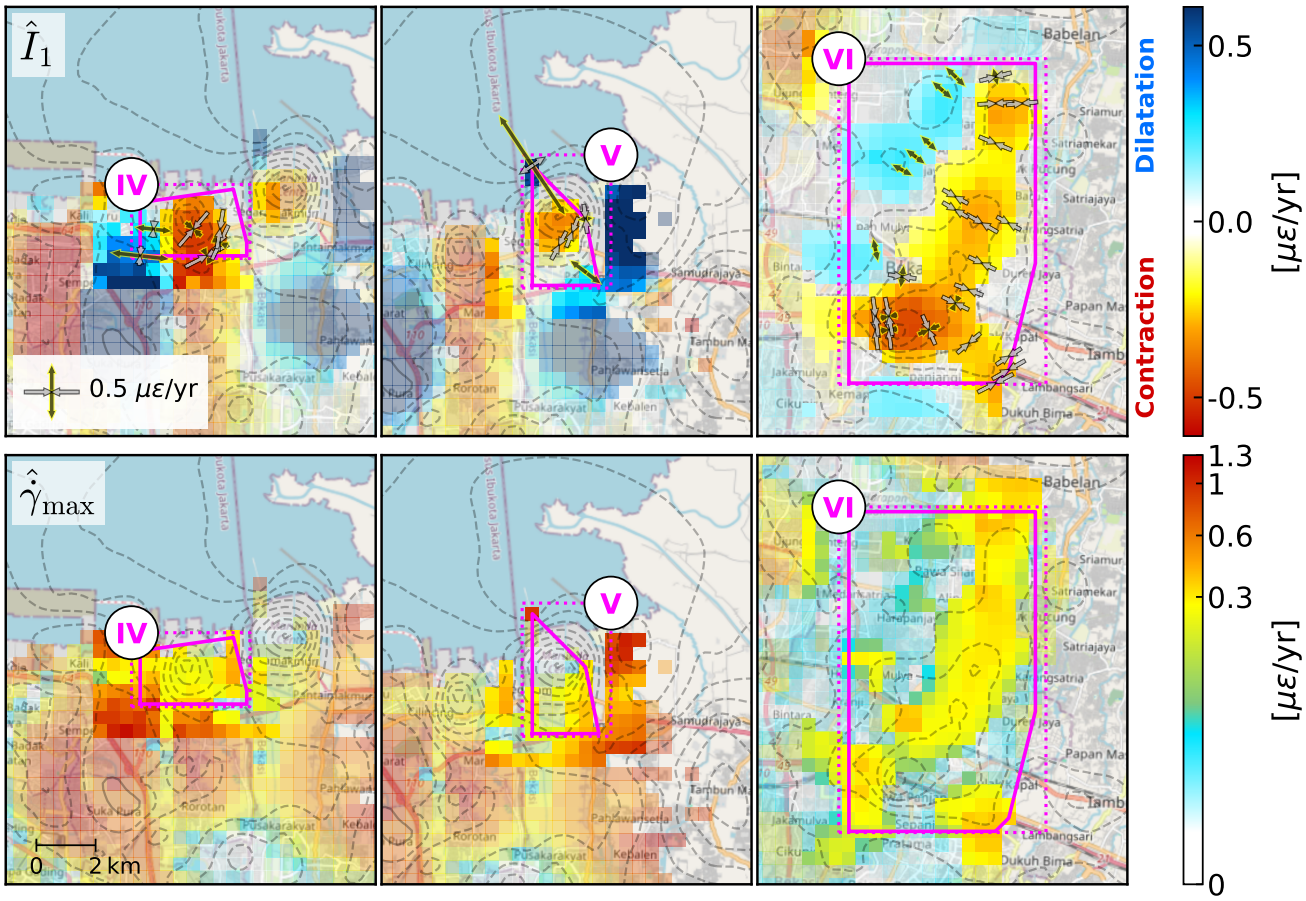


Figure S1. Close-up of the Jakarta strain-rate maps in Fig. 4, showing the estimated first strain-rate invariant $\hat{I}_1$ with principal strain-rate glyphs (top row) and maximum engineering shear strain rate $\hat{\dot{\gamma}}_{max}$ (bottom row) in subsidence regions IV, V, and the southern part of region VI (left to right). Magenta outlines delimit the regions. These regions show center-to-flank contraction→shear→dilatation patterns, similar to that observed in the southern part of region II, consistent with bowl-shaped subsidence.